

## MAGNETIC FIELD STRUCTURES IN AND AROUND SEYFERT GALAXY OUTFLOWS

SALMOLI GHOSH,<sup>1</sup> PREETI KHARB,<sup>1</sup> BINY SEBASTIAN,<sup>2,3</sup> JACK GALLIMORE,<sup>4</sup> ALICE PASETTO,<sup>5</sup> CHRISTOPHER P. O'DEA,<sup>2</sup>  
TIMOTHY HECKMAN,<sup>6</sup> AND STEFI A. BAUM<sup>2</sup>

<sup>1</sup>*National Centre for Radio Astrophysics (NCRA) - Tata Institute of Fundamental Research (TIFR), S. P. Pune University Campus, Pune 411007, Maharashtra, India*

<sup>2</sup>*Department of Physics and Astronomy, University of Manitoba, Winnipeg, Manitoba, Canada*

<sup>3</sup>*Space Telescope Science Institute, 3700 San Martin Drive, Baltimore, MD 21218, USA*

<sup>4</sup>*Department of Physics and Astronomy, Bucknell University, Lewisburg, PA 17837*

<sup>5</sup>*Instituto de Radioastronomía y Astrofísica (IRyA-UNAM), 3-72 (Xangari), 8701, Morelia, Mexico*

<sup>6</sup>*William H. Miller III Department of Physics & Astronomy, Johns Hopkins University, Bloomberg Center for Physics and Astronomy, 3400 N. Charles Street, Baltimore, MD 21218, USA*

### ABSTRACT

We present radio polarimetric images of 12 Seyfert and Low-Ionization Nuclear Emission-line Region (LINER) galaxies belonging to the Centre for Astrophysics (CfA)+12 micron sample exhibiting kiloparsec-scale radio outflows (KSRs). These observations have been carried out at 10 GHz with Karl G. Jansky Very Large Array (VLA) in D-array and at 1.4 GHz with the BnA→A array configurations. We find signatures of organized magnetic (B-) field structures in the cores, jets and lobes of these galaxies. The linear polarization fraction varies from a few per cent in the cores to  $47 \pm 18$  per cent in the lobes. The inferred B-fields are toroidal in the cores of several sources making them consistent with the presence of either a sheath-like or a wind-like component surrounding the jet. The in-band spectral index images typically show the presence of flat/inverted spectrum cores and steep spectrum lobes. Radio cores with flatter spectra are found to have lower Eddington ratios while the steeper ones have higher. A strong correlation is observed between the Seyfert/LINER radio outflow properties and the mass of the supermassive black holes (SMBHs); correlations with Eddington ratios are weaker. We find signatures of jet-medium interaction and both positive and negative AGN feedback in these sources. Overall, our study indicates that radio-quiet (RQ) AGN with KSRs possess radio outflows driven by magnetic fields anchored to their black holes - accretion disks, which significantly impact their environments.

arXiv:2501.08141v1 [astro-ph.GA] 14 Jan 2025

## 1. INTRODUCTION

Seyfert galaxies (Seyfert 1943) were the first identified class of galaxies known to host active galactic nuclei (AGN), a phenomenon now understood to result from mass accretion onto supermassive black holes (SMBH) (Rees 1984). Seyferts are known to host SMBH of lower masses, typically ranging from  $M \sim 10^6 - 10^8 M_\odot$  (McLure & Dunlop 2001). They are traditionally classified as radio-quiet (RQ) AGN (Padovani 2017; Panessa et al. 2019), characterized by a ratio of radio flux density at 5 GHz to optical flux density in the B-band of  $\leq 10$  (Kellermann et al. 1989). These galaxies exhibit high ionization emission lines in their optical and UV spectra and are typically found in spiral, lenticular or irregular host galaxies (Peterson 1997). Low-Ionisation Nuclear Emission-line Region (LINER) galaxies show relatively lower ionization emission lines in their spectra (Heckman 1980; Ho 1996). They are typically distinguished by lower  $[\text{OIII}]\lambda 5007/\text{H}\beta$  values for similar  $[\text{NII}]\lambda 6593/\text{H}\alpha$  values in the Baldwin Phillips Terlevich (BPT) diagram (Baldwin et al. 1981). Seyfert and LINERs are categorized as low-luminosity AGN, indicating lower levels of accretion activity compared to more luminous AGN (Peterson 1997; Nagar et al. 2002a; Maoz 2007).

In roughly one-fourth of the Seyfert galaxies, the toroidal dusty region surrounding the black-hole-accretion-disk system obscures the faster-moving dense clouds called the broad line region (BLR;  $n_e > 10^9 \text{ cm}^{-3}$ ,  $v < 10^4 \text{ km s}^{-1}$ ) from certain lines of sight giving rise to type 2 Seyferts (Peterson 1997; Ho 1999). When both the BLR and the slower-moving less-dense clouds, which are further away from the black hole - accretion disk system, also known as the narrow line region (NLR;  $n_e \approx 10^3 - 10^6 \text{ cm}^{-3}$ ,  $v \sim 100 \text{ km s}^{-1}$ ), remain visible from our line of sight, they are identified as type 1 Seyferts (Antonucci 1993; Urry & Padovani 1995a; Peterson 1997). Type 2 Seyfert galaxies sometimes show broad lines in polarized light revealing the dust obscured BLR (e.g., Tran et al. 1992; Nagao et al. 2004), consistent with the picture of Unified Model (Antonucci 1993; Urry & Padovani 1995b).

After radio interferometric imaging became routine in the 1960s and 1970s, it was clear that Seyfert galaxies hosted smaller radio structures that typically stayed confined to their spiral or lenticular host galaxies (de Bruyn & Wilson 1976; Wilson & Willis 1980). Later, a population of Seyferts was identified with relativistic jets (e.g., Abdo et al. 2009; Foschini 2012; Lähteenmäki et al. 2018), adding complexity to the conventional view of Seyferts as predominantly low-power, RQ AGN. Recently,  $\sim 100$  kpc-scale jets have been observed in a few Seyferts (Vietri et al. 2022; Chen et al. 2024), and su-

perluminal jet motion has been reported in KISSR 872 (Kharb et al. 2024). A sensitive radio survey of Seyferts and LINERs with the VLA D-array at 5 GHz has detected kpc-scale radio outflows (KSRs) not associated with the optical emission from the host galaxies in at least  $\approx 40\%$  of the RQ sources in a complete sample (Gallimore et al. 2006a). There has been extensive debate about the origin and nature of the radio emission observed in Seyfert/LINER galaxies: AGN-driven jets or winds (e.g., Colbert et al. 1996a; Gallimore et al. 2006a; Kharb et al. 2006), starburst-driven winds (e.g., Baum et al. 1993), coronal winds, gas powered by shocks (Heckman 1987; Filippenko 1992; Panessa et al. 2019; Fischer et al. 2023), or a combination of these (e.g., Singh et al. 2015) are the suggested contenders. Very long baseline interferometry (VLBI) observations that probe milli-arcsecond (mas) scales and hundred mas-scale with telescopes like the Very Long Baseline Array (VLBA), the European VLBI Network (EVN) and the Multi-Element Radio Linked Interferometer Network (MERLIN), have revealed tenuous connections between AGN jet emission on parsec-scales to the KSRs, in a few Seyfert galaxies (e.g., Mrk 6, NGC 6764; Kharb et al. 2010, 2014, respectively), though have been opposed by other studies (e.g., NGC 1068; Fischer et al. 2023).

In this paper, we have investigated the extended polarized radio structures of Seyfert and LINER galaxies on kpc-scales. More organized magnetic field structures are expected in the AGN outflows compared to the synchrotron emission associated with starburst activity (Panessa et al. 2019; Sebastian et al. 2020). However, disentangling the contributions of AGN jets and winds from the galactic synchrotron emission is challenging (e.g., Silpa et al. 2021b). Mehdipour & Costantini (2019) suggest that in RQ AGN, the jets typically exhibit poloidal magnetic fields aligned with them, while the winds have toroidal magnetic fields perpendicular to the flow direction. We have analyzed polarized emission from these galaxies to elucidate the origin, propagation, and interaction of the radio outflows with the surrounding media. This work follows the 5 GHz VLA B-array study on Seyfert galaxies by Sebastian et al. (2020). Higher frequency observations were obtained to partially discount the effects of Faraday rotation induced depolarization. The D-array was chosen for improving the sensitivity to diffuse lobe emission in these galaxies (as well as galactic emission in NGC 4388)<sup>1</sup>. Additionally,

<sup>1</sup> Two sample sources presented here, viz., NGC 1068 and NGC 1320 were part of the previous 1.4 GHz VLA study of Seyfert galaxies (Project 21B-291).

**Table 1.** Properties of the CfA+12 micron Seyfert & LINER Sample

Source	Alternate	Type	R.A.	Dec.	Redshift	$\log(M_{\text{BH}})$	$\log(L_{\text{bol}})$	$\log(\lambda_{\text{Edd}})$	$\log R$
name	name		J2000	J2000		$(M/M_{\odot})$	$(\text{erg s}^{-1})$		
			hh mm ss.ss	dd mm ss.ss					
NGC 262	Mrk 348	Seyfert 2, KSR	00 48 47.14	+31 57 25.08	0.01503	7.21 <sup>[1]</sup>	44.27 <sup>[1]</sup>	-1.04	-0.92 <sup>[8]</sup>
Mrk 993	UGC 00987	Seyfert 2, point	01 25 31.46	+32 08 11.43	0.01553	...	...	...	...
IRAS 01475-0740	...	Seyfert 2, KSR	01 50 02.69	-07 25 48.48	0.01767	6.09 <sup>[8]</sup>	44.33	0.14 <sup>[8]</sup>	-0.79 <sup>[8]</sup>
NGC 1068	M 77	Seyfert 2, KSR	02 42 40.71	-00 00 47.81	0.00379	7.23 <sup>[1]</sup>	44.98 <sup>[1]</sup>	-0.35	-2.47 <sup>[8]</sup>
NGC 1194	UGC 02514	Seyfert 1, point	03 03 49.11	-01 06 13.48	0.01363	7.32 <sup>[8]</sup>	...	-1.02 <sup>[8]</sup>	-3.27 <sup>[8]</sup>
NGC 1241	...	Seyfert 2, KSR	03 11 14.64	-08 55 19.7	0.01343	...	...	...	...
NGC 1320	Mrk 607	Seyfert 2, KSR	03 24 48.70	-03 02 32.20	0.00928	7.18 <sup>[1]</sup>	44.02 <sup>[1]</sup>	-1.26	-3.58 <sup>[8]</sup>
IRAS 04385-0828	...	Seyfert 2, point	04 40 54.96	-08 22 22.23	0.0151	8.77 <sup>[8]</sup>	...	-2.44 <sup>[8]</sup>	-2.27 <sup>[8]</sup>
Mrk 9	...	Seyfert 1.5, point	07 36 56.97	+58 46 13.43	0.03914	7.46 <sup>[8]</sup>	...	-0.62 <sup>[8]</sup>	-2.92 <sup>[8]</sup>
NGC 2639	UGC 04544	LINER 1.9, KSR	08 43 38.07	50 12 20.00	0.011128	7.9 <sup>[2]</sup>	42.61 <sup>[3]</sup>	-3.39	-0.48 <sup>[8]</sup>
NGC 2992	IRAS 09432-1405	Seyfert 2, KSR	09 45 42.05	-14 19 34.98	0.007710	7.72 <sup>[1]</sup>	43.92 <sup>[1]</sup>	-1.90	-2.48 <sup>[8]</sup>
NGC 3079	UGC 05387	LINER, KSR	10 01 57.80	+55 40 47.24	0.003689	7.97 <sup>[8]</sup>	43.68	-2.39 <sup>[8]</sup>	-1.66 <sup>[8]</sup>
NGC 3516	UGC 06153	Seyfert 1, KSR	11 06 47.49	+72 34 06.88	0.008836	7.36 <sup>[1]</sup>	44.29 <sup>[1]</sup>	-1.17	-3.16 <sup>[8]</sup>
NGC 4051	UGC 07030	Seyfert 1.5, KSR	12 03 09.61	+44 31 52.80	0.002336	6.13 <sup>[1]</sup>	43.56 <sup>[1]</sup>	-0.67	-3.80 <sup>[8]</sup>
NGC 4151	UGC 07166	Seyfert 1, KSR	12 10 32.58	+39 24 20.63	0.00884	7.13 <sup>[1]</sup>	43.73 <sup>[1]</sup>	-1.50	-2.61 <sup>[8]</sup>
NGC 4235	UGC 07310	Seyfert 1, KSR	12 17 09.88	+07 11 29.67	0.007548	7.4 <sup>[2]</sup>	42.54 <sup>[4]</sup>	-2.96	-1.74 <sup>[9]</sup>
NGC 4388	UGC 07520	Seyfert 1, KSR	12 25 46.74	+12 39 43.51	0.008419	6.92 <sup>[5]</sup>	44.40 <sup>[5]</sup>	-0.62	-3.50 <sup>[8]</sup>
NGC 4593	Mrk 1330	Seyfert 1, KSR	12 39 39.42	-05 20 39.34	0.008312	6.91 <sup>[1]</sup>	44.09 <sup>[1]</sup>	-0.92	-2.81 <sup>[9]</sup>
NGC 4594	M 104/Sombrero	LINER 1.9, KSR	12 39 59.43	-11 37 22.99	0.003639	8.9 <sup>[2]</sup>	42.15 <sup>[4]</sup>	-4.85	...
NGC 5283	Mrk 270	Seyfert 2, point	13 41 05.76	+67 40 20.32	0.01014	7.6 <sup>[1]</sup>	43.37 <sup>[1]</sup>	-2.33	...
NGC 5273	UGC 08675	Seyfert 1.9, point	13 42 08.34	+35 39 15.17	0.00361	6.51 <sup>[1]</sup>	43.03 <sup>[1]</sup>	-1.58	...
NGC 5347	UGC 08805	Seyfert 2, KSR	13 53 17.83	+33 29 26.98	0.007899	6.79 <sup>[1]</sup>	43.81 <sup>[1]</sup>	-1.08	...
NGC 5506	Mrk 1376	Seyfert 1.9, KSR	14 13 14.89	-03 12 27.28	0.006084	7.94 <sup>[6]</sup>	44.02 <sup>[7]</sup>	-2.02	-2.35 <sup>[8]</sup>
NGC 5548	Mrk 1509/9027	Seyfert 1.5, KSR	14 17 59.53	+25 08 12.44	0.01717	8.03 <sup>[1]</sup>	44.83 <sup>[1]</sup>	-2.30	-2.91 <sup>[8]</sup>
NGC 5695	Mrk 686	Seyfert 2, KSR	14 37 22.12	+36 34 04.11	0.01415	...	...	...	...
NGC 5929	I Zw 112	Seyfert 2, KSR	15 26 06.16	+41 40 14.40	0.00851	7.25 <sup>[1]</sup>	43.04 <sup>[1]</sup>	-2.31	-1.70 <sup>[8]</sup>

Columns 1 & 2: Source names. Column 3: Spectral type and radio morphology. Column 4, 5 & 6: RA, Dec and redshifts of the sources. Column 7: Logarithm of the black hole masses. Column 8: Logarithm of the bolometric luminosities in  $\text{erg s}^{-1}$ . Column 9: Logarithm of the Eddington ratios. Column 10: Logarithm of the radio loudness parameter. References: [1] Woo & Urry (2002) [2] Dong & De Robertis (2006) [3] using [OIII] line fluxes from [2] and using the relations from Heckman et al. (2004) [4] Kharb et al. (2016) [5] Ursini et al. (2019) [6] Nikolajuk et al. (2009) [7] Matt et al. (2015) [8] Meléndez et al. (2010) [9] Obtained by dividing total radio luminosity (excluding galactic emission) extrapolated to 8.4 GHz by the [OIV] $\lambda$ 25.89  $\mu\text{m}$  line luminosity from Weaver et al. (2010).

we have investigated the radio spectral indices to understand the particle emission mechanisms. Emission-line data from a few nearby sources are examined to look for possible correlations with the polarized radio emission.

The paper consists of the following sections. Section 2 discusses the details of the selected sample for this study. Section 3 describes the observational details and data reduction procedures. Section 4 reports the results obtained from the data analysis with sections 4.1, 4.2, 4.3, and 4.4 presenting the details of individual sources, AGN jet powers, energetics, and correlations found for the sample sources, respectively. Section 5 focuses on the interpretations and impact of our results. Finally, section 6 summarises the paper.

In this paper, the spectral index  $\alpha$  is defined such that flux density at a frequency  $\nu$  is  $S_{\nu} \propto \nu^{\alpha}$ . The adopted cosmology is  $H_0 = 67.8 \text{ km s}^{-1} \text{ Mpc}^{-1}$ ,  $\Omega_{\text{mat}} = 0.308$ ,  $\Omega_{\text{vac}} = 0.692$ . By way of a definition, we have considered a radio outflow to be a ‘jet’ if its length exceeds its width by a factor of at least 2.5. This suggestion follows from a similar one made for RL sources by Bridle et al. (1994). If the jet is not delineated, then a spectral index gradient or ordered polarization vectors are used for inferring its presence.

## 2. THE SAMPLE

The parent sample for this study comprises 26 Seyfert and LINER galaxies belonging to the Center for Astrophysics (CfA; Huchra & Burg 1992) and the extended 12 micron (Rush et al. 1993) sample. These sources were known to exhibit either a ‘KSR’ or a compact component identified as ‘point sources’ in the VLA study of Gallimore et al. (2006a). The sources have a redshift cutoff of  $cz \leq 5149 \text{ km s}^{-1}$  ( $z \lesssim 0.02$ ) to resolve the KSRs of about 7 kpc from the radio nucleus, and declination  $> 20^\circ$  for observing with the VLA. Out of the 40 sources in Gallimore et al. (2006a), we excluded 14 galaxies whose radio continuum matched the optical disk closely, resulting in a sample of 26 galaxies hosting either a type 1 or a type 2 AGN (Seyferts and LINERs), thus decreasing the probability of the radio emission being powered by stellar activity in the selected sample. The sample with some basic properties is presented in Table 1.

In this paper, we present polarization-sensitive images along with the spectral index images of a sub-sample of 12 galaxies, from the sample of 26 (Table 2), identified as having KSRs, at 10 GHz with VLA D-array configuration with a bandwidth of 4 GHz and a resolution

of  $\sim 7''$  (Project ID: 19B-198; PI: Biny Sebastian), as well as 1.4 GHz with the VLA BnA→A array configurations with a bandwidth of 1 GHz and a resolution of  $\sim 2''$  (Project ID: 21B-291; PI: Biny Sebastian). An additional dataset at 5.5 GHz from the VLA D-array from project 21B-291 has been analysed for one particular source (NGC 4388). Three sources have been classified as LINER galaxies while nine are Seyfert galaxies of both type 1 and 2. The redshift distribution of the sources with respect to the total 1.4 GHz radio luminosity from the NRAO VLA Sky Survey (NVSS; [Condon et al. 1998](#)) is shown in Figure 1. The different coloured markers are representative of different galaxies and this convention is followed in the subsequent plots. Polarization data of the remaining sample (14 of 26) sources have been recently acquired and will be the subject of another paper.

We have defined the radio loudness parameter ( $R$ ) as the ratio of 8.4 GHz radio flux density to  $[\text{OIV}]\lambda 25.89 \mu\text{m}$  line flux density as defined by [Meléndez et al. \(2010\)](#). This provides a more accurate measure of radio-loudness being unaffected by dust extinction as observed in other methods involving optical observations. We note that for our sample sources, the adopted  $R$  parameter did not alter the designation of the sources into the RL and RQ categories, as obtained from the original definition of [Kellermann et al. \(1989\)](#) as used by [Rush et al. \(1996\)](#). In the cases where the 8.4 GHz flux density was unavailable, the  $R$  was calculated at 8.4 GHz by extrapolating its total radio luminosity at 10 GHz with its corresponding spectral index value, divided by its  $[\text{OIV}]\lambda 25.89 \mu\text{m}$  line flux densities obtained from [Weaver et al. \(2010\)](#).

### 3. RADIO DATA ANALYSIS

Polarization-sensitive data were acquired with VLA ([Thompson et al. 1980](#)) D-array and BnA→A array configurations at 10 GHz and 1.4 GHz, respectively. The observations were carried out in November 2019 with two sources observed in February - March 2022. Details of the observations and a list of calibrators are provided in Table 2. For the data analysis, the basic calibrations were carried out using the VLA recipes for Common Astronomical Software Application (CASA; [THE CASA TEAM et al. 2022](#), version 6.6). This includes flagging, pre-determined calibrations like antenna position corrections and atmospheric opacity corrections, an iterative initial delay, bandpass, and gain calibrations. These are followed by additional flagging of the bad data, deriving the final delay and bandpass, obtaining the gain calibration solutions, and applying them to the data.

Polarization calibration was carried out following the CASA-based polarization script<sup>2</sup>. The polarization calibration primarily includes three steps: solving for the cross-hand delay, solving for the leakage terms, and solving for the polarization angle. For most cases, the polarized calibrator i.e., 3C 286 or 3C 138, observed over a large parallactic angle range ( $\sim 60^\circ$ ), has been used to derive the leakages. In some cases, the unpolarized calibrator i.e., OQ 208 or 3C 84 has been used if the leakage solutions showed less scatter using the unpolarized ones. The leakages obtained for the VLA antennas were typically 5% or less. For the delay and polarization angle calibration, polarized calibrator (3C 138 or 3C 286) with known polarization angles has been used.

After applying these calibration solutions to the data, it was averaged over every  $\sim 8$  channels to reduce the data volume. The target sources were then imaged using MULTI-TERM MULTI-FREQUENCY SYNTHESIS (mtmfs [Rau & Cornwell 2011](#)) deconvolver, and ‘BRIGGS’ weighting with different robust parameters according to the requirement of weighting the longer or shorter baselines’ data. MTMFS was run with terms = 2 to find out the in-band  $\alpha$  at each pixel apart from the flux densities. A few rounds of phase-only and amplitude + phase self-calibration were carried out on the Stokes I images till convergence. The calibration results were applied to the data, and then the Stokes I, Q, U, and V images were obtained from the self-calibrated data. The in-band spectral index image is obtained by blanking the spectral index image with its error image using an appropriate cut-off, which typically turns out to be  $> 30\%$ . The post-imaging analyses were carried out using Astronomical Image Processing System (AIPS; [van Moorsel et al. 1996](#)), CASA and PYTHON. The r.m.s. noise levels obtained for each image have been tabulated in Table 2.

The linear polarization intensity ( $I_p$ ), fractional polarization ( $f_p$ ), polarization angle ( $\chi$ ) values were obtained as  $\sqrt{Q^2 + U^2}$ ,  $\sqrt{Q^2 + U^2}/I$ , and  $0.5 \tan^{-1}(U/Q)$ . The  $I_p$  images were generated in AIPS using task COMB opcode POLC, which accounts for the Ricean bias corrections, with a  $3\sigma$  cut-off. The  $\chi$  values were obtained with opcode POLA and a  $10^\circ$  angle error cut-off. The  $f_p$  images were made by dividing the  $I_p$  values with the I values, blanking with the 10% error cut-off. The final electric vector position angle (EVPA) images were obtained by plotting the vectors with lengths proportional to  $f_p$  and angle  $\chi$ . For optically thin synchrotron emission, the inferred magnetic field (B-field) is per-

<sup>2</sup> [https://github.com/astrouser-salm/radio-imaging/blob/main/VLA\\_polarization\\_pipeline.py](https://github.com/astrouser-salm/radio-imaging/blob/main/VLA_polarization_pipeline.py)

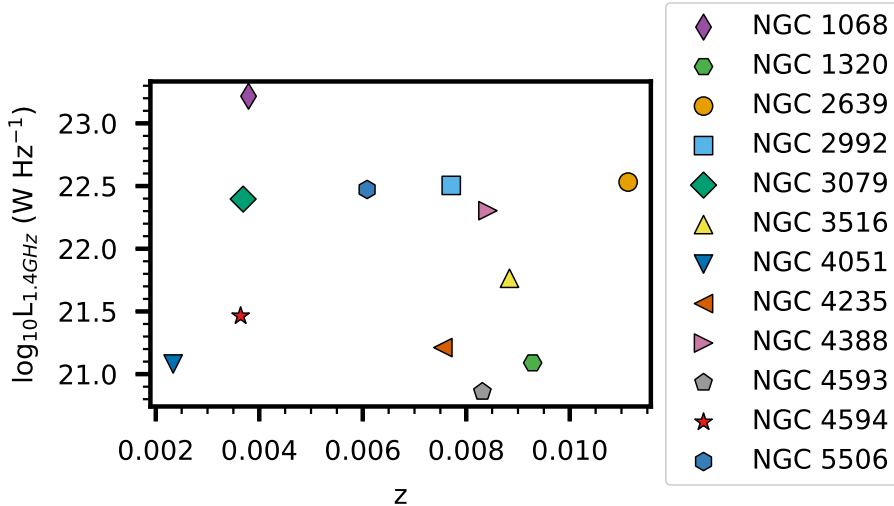


**Figure 1.** Redshift distribution of the sample presented in this paper with their corresponding VLA NVSS 1.4 GHz radio luminosities. Each Seyfert and LINER galaxy has been assigned a coloured marker that is preserved in the subsequent plots.

pendicular to the observed EVPAs (Pacholczyk 1970; Contopoulos et al. 2015). Conversely, in optically thick regions (with optical depth  $\tau \gtrsim 6$  and spectral index  $\alpha \gtrsim 0.5$ ), inferred B-field vectors are parallel to the EVPAs (Cawthorne & Hughes 2013; Wardle 2018). Therefore, for radio cores with an inverted spectrum with  $\alpha \geq 0.5$ , we interpret the B-fields to be aligned with the EVPAs. In all other situations, the B-fields are perpendicular to the EVPAs.

For estimating the core flux densities, we have obtained the peak intensity values (in  $\text{mJy beam}^{-1}$ ) by fitting each core with a Gaussian component. We considered the peak intensity values to be representative of the flux density for the compact core components. For the extended lobes/jets, the flux densities are obtained in  $\text{mJy}$  for the entire region. Mean values were obtained using CASA’s polygon selector tool and running statistical analysis on the selected region. The errors in flux densities for the extended regions are derived by  $\sqrt{(\sigma\sqrt{N_b})^2 + (\sigma_p S)^2}$  (Kale et al. 2019), where  $S$  is the flux density,  $\sigma_p$  is the percentage error in flux density (a conservative 5% error is considered),  $\sigma$  is the r.m.s. noise of the image,  $N_b$  is the number of beams in the region. Estimates of the core spectral index  $\alpha$ , polarization fraction ( $f_p$ ), and polarization angle ( $\chi$ ) were obtained as average values in a box roughly equivalent to the FWHM of the synthesized beam centred on the core.

With the VLA D-array at 10 GHz, and BnA→A array at 1.4 GHz, we observed 10 sources at a resolution of  $\sim 7''$  and 2 sources (NGC 1068, NGC 1320) at a resolution of  $\sim 2''$ , respectively. Considering the redshift range of this sample ( $z = 0.002 - 0.01$ ), the smallest spatial scales probed are between 300 pc and 1.5 kpc

with D-array at 10 GHz and 85 pc to 500 pc with BnA array at 1.4 GHz, respectively. We note that while the ‘core’ sizes are smaller in the  $2''$ -scale versus the  $7''$ -scale images, convolving the  $2''$ -scale images with  $7''$  beams using IMSMOOTH in CASA resulted in similar core flux densities as obtained previously with the peak flux estimates at  $2''$  for the cores of the two sources. The peak flux is off by a factor of about 1.3 due to the inclusion of diffuse jet or lobe emission when convolved with the larger beam. We have therefore retained the original resolutions of the images for defining the ‘cores’.

## 4. RESULTS

The VLA  $\sim 7''$  images reveal extended features or lobe emission in all sample galaxies except NGC 2639 and NGC 4593; extended lobe emission in these sources, if any, are on scales smaller than those probed in our observations. In four galaxies, viz., NGC 4388, NGC 3079, NGC 4594, and NGC 1068, radio emission from the host galaxy is also detected (see Figure 21 in the APPENDIX). Linear polarization is detected in the cores, jets or lobes for all the 12 Seyfert and LINER galaxies. Below we discuss the results for individual sources.

### 4.1. Notes on Individual Sources

#### 4.1.1. NGC 1068

NGC 1068 is a well-known spiral galaxy identified early-on to host a Seyfert nucleus. It later classified as a type 2 Seyfert due to the presence of an obscured BLR (Khachikian & Weedman 1974; Antonucci & Miller 1985). The AGN in this source has been suggested to drive a biconical molecular outflow almost perpendicular to the nuclear disk causing a deficit of molecular gas at the central 130 pc, leaving out only a 400 parsec

**Table 2.** Observational Details.

Source	Observation Date	Frequency GHz	VLA Array Configuration	r.m.s. noise ( $\mu\text{Jy}/\text{beam}$ )	Polarization Angle Calibrator	Leakage Calibrator
NGC 1068	26-Feb-2022	1.4	BnA→A	250	3C 138	3C 138
NGC 1320	03-Mar-2022	1.4	BnA→A	40	3C 138	3C 138
NGC 2639	11-Nov-2019	10	D	15	3C 138	3C 84
NGC 2992	10-Nov-2019	10	D	12	3C 138	3C 84
NGC 3079	08-Nov-2019	10	D	30	3C 286	3C 286 & OQ 208
NGC 3516	09-Nov-2019	10	D	16	3C 286	3C 286 & OQ 208
NGC 4051	11-Nov-2019	10	D	15	3C 286	3C 286 & OQ 208
NGC 4235	08-Nov-2019	10	D	15	3C 286	3C 286 & OQ 208
NGC 4388	20-Nov-2019	10	D	20	3C 286	3C 286 & OQ 208
NGC 4388	11-Nov-2019	5.5	D	17	3C 286	3C 286 & OQ 208
NGC 4593	12-Nov-2019	10	D	45	3C 286	3C 286 & OQ 208
NGC 4594	10-Nov-2019	10	D	22	3C 286	3C 286 & OQ 208
NGC 5506	08-Nov-2019	10	D	9	3C 286	3C 286 & OQ 208

sized, ring-shaped circumnuclear disk (Gallimore et al. 2016; García-Burillo et al. 2024). The high-resolution images of this source show a  $\sim 13''$  ( $\sim 0.8$  kpc) linearly oriented jet-like structure from the core ending at a bow-shock-like edge (Wilson & Ulvestad 1982; Ulvestad et al. 1987).

Our observations reveal both the galactic disk emission and the Seyfert outflow at the center. The galactic emission is most likely due to synchrotron radiation from supernova remnants associated with starburst activity (Wilson & Ulvestad 1982). The Seyfert emission extends approximately  $26''$  ( $\sim 1.7$  kpc). We observe an offset in the polarization angle at the northern bowshock or hotspot in the Seyfert outflow at 1.4 GHz compared to that found by Wilson & Ulvestad (1982) at 15 GHz (see Figure 2, top panel). This offset can be attributed to the RM, which is more significant at lower frequencies.

The in-band spectral index image centered around 1 GHz (see Figure 2, bottom panel) presents a jet-core-jet structure with a steep spectrum core ( $\alpha \approx -0.67$ ) and an even steeper spectrum jet/outflow ( $\alpha \approx -0.88$ ). A new feature towards the east of the core is highlighted in polarized emission, exhibiting a high polarization fraction of  $f_p = 3.2 \pm 0.4\%$ . Interestingly, the spectral index image reveals that this highly polarized region has a flat spectrum ( $\alpha \approx 0$ ) with a  $24\sigma$  detection in total intensity and an error of 0.001 in the spectral index. This region may result from the sweeping away of relic radio plasma by ram-pressure bending along the galaxy’s spiral motion (see Kapferer et al. 2009). Ram-pressure on

relic plasma may have re-energized the charged particles (see Lebedev et al. 2014) flattening the spectrum (e.g., Kang & Ryu 2011, for galaxy cluster environments).

#### 4.1.2. NGC 1320

NGC 1320 is an edge-on spiral galaxy with a Seyfert type 2 nucleus having narrow emission lines (De Robertis & Osterbrock 1986). Faint radio emission ( $\sim 3.5$  mJy at 5 GHz) of extent 0.9 kpc and 2.6 kpc towards the south from the core was observed by Colbert et al. (1996a) and Gallimore et al. (2006a), respectively. We detect a clearer core-lobe structure with emission clearly extended to the north-south as well as the north-east. A total flux density of 5.6 mJy at 1.5 GHz and a total radio extent of  $\sim 9.7''$  ( $\sim 2$  kpc) is detected in this  $\sim 2''$  ( $\sim 370$  pc) resolution image. High fractional polarization ( $47 \pm 18\%$ ) is observed at the end of the southern lobe (Figure 3, left panel). Fractional polarization of  $20 \pm 6\%$  is observed to the north of the core. The [OIII] $\lambda 5007$  emission as observed by Schmitt et al. (2003) is concentrated at the core and has an extent of  $\sim 660$  pc in the north-west direction, which also coincides with the host galaxy major axis (see Ferruit et al. 2000).

The spectral index image (Figure 3, right panel) suggests that the true core (with a flatter spectral index) is to the west of the peak emission and that the jet emerges to the south-east before bending towards the south. Overall, an S-shape is observed in the north-south jet and the inferred magnetic fields are aligned with the radio outflow both in the north and south. The origin of the extended emission to the north-east is unclear.

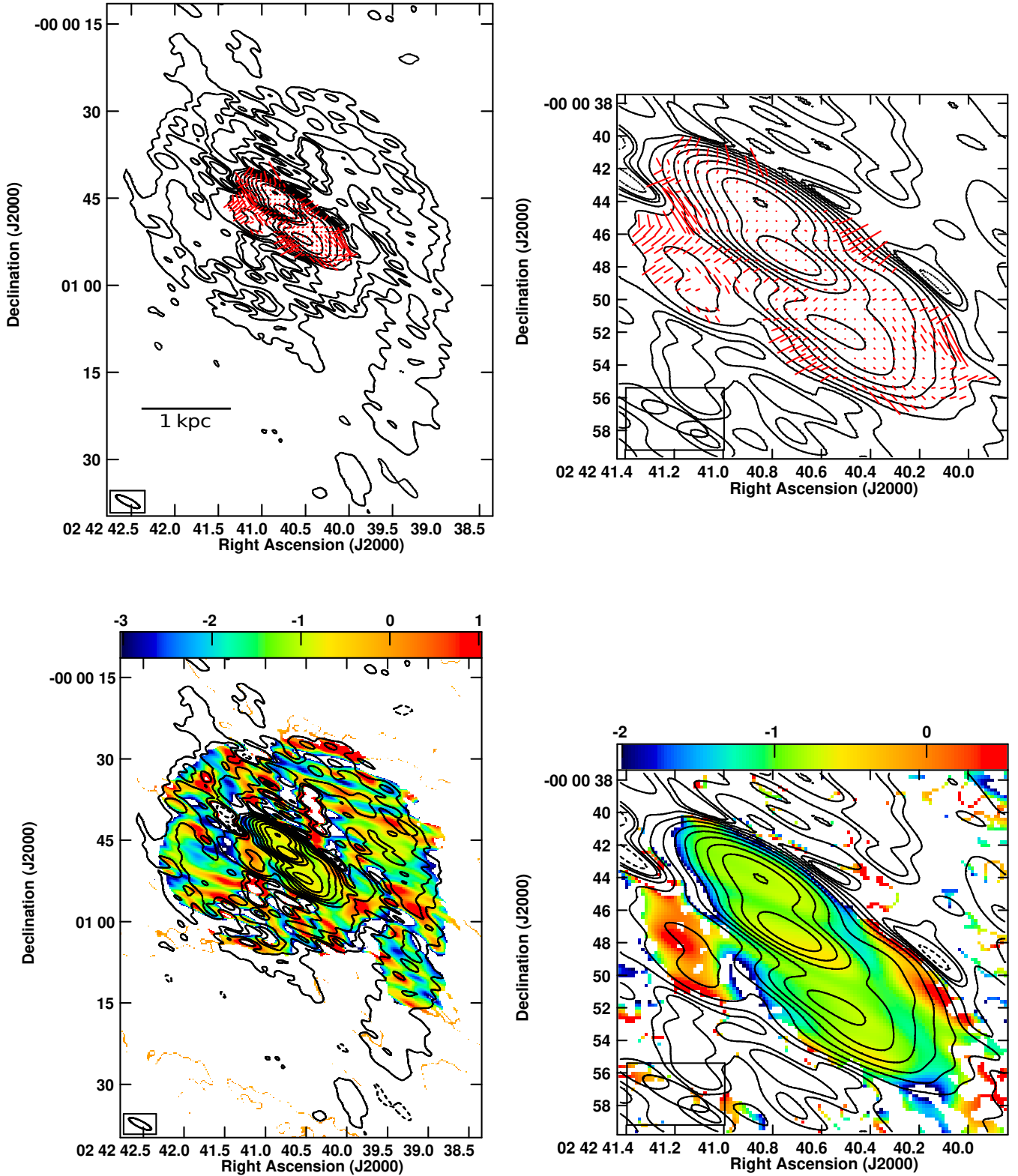


**Figure 2.** (Top left) NGC 1068 image at 1.52 GHz with the VLA BnA→A array at a resolution of  $\sim 2''$ . The contour levels in all the panels are at  $3\sigma \times (-1, 1, 2, 4, 8, 16, 32, 64, 128, 256, 512, 1024)$  with  $\sigma = 250 \mu\text{Jy beam}^{-1}$ . Similarly, the synthesized beam size is  $4.57'' \times 1.23''$  at a position angle (PA) of  $63.8^\circ$ . The tick lengths are proportional to fractional polarization with 5 arcsec = 15.6%. *Radio emission is detected from the host galaxy along with the KSR.* (Top right) Zoomed-in image showing the KSR. The tick lengths are proportional to fractional polarization with 4 arcsec = 25%. (Bottom left) In-band spectral index image of NGC 1068. The spectral index values in colour range from  $-3.0$  to  $+1.0$ . (Bottom right) Zoomed-in image showing the KSR. The spectral index values in colour range from  $-2.0$  to  $+0.5$ .

#### 4.1.3. NGC 2639

NGC 2639 is a spiral galaxy with an extension of  $\sim 60$  kpc possessing both inner and outer rings, hosting a Seyfert 1.9 or a LINER nucleus (Véron-Cetty & Véron 2006). Xanthopoulos et al. (2010) identified an S-shaped bent morphology in the radio emission from this source at 5 GHz, suggesting jet precession along with strong jet-medium interaction impeding jet propagation. However, Sebastian et al. (2019b) later ruled out jet precession for this source and discovered episodic activity, with earlier episodes exhibiting greater extents than previously reported. Recently, the source has been observed to undergo multiple episodes of activity, exhibiting the highest frequency of such episodes among Seyferts, as evidenced by observations at various frequencies and resolutions (Rao et al. 2023).

At a resolution of  $\sim 7''$  ( $\sim 2$  kpc) at 10 GHz, the Seyfert outflow of extent of  $32''$  ( $\sim 8$  kpc) is not resolved into individual features. The structure resembles the Giant Metrewave Radio Telescope (GMRT) 325 MHz image of this source (Rao et al. 2023), which is considered to originate from the first episode of activity. The inferred B-field, perpendicular to the EVPAs shown in Figure 4 (left panel), is oriented along the northeast direction in the central region of the source, suggesting a jet-like structure in that direction. This is confirmed by the GMRT 735 MHz image (resolution  $\sim 5''$ ; Rao et al. 2023), which reveals a jet along the same direction.

The spectral index image (Figure 4; right panel) shows a gradient perpendicular to the jet direction with flat ( $\alpha \sim 0$ ) to inverted ( $\alpha \sim 0.5$ ) spectral index values. This may be because the source hosts multiple radio lobes in different directions, sometimes perpendicular to each other, with the newest episode being oriented along the northwest-southeast direction. The positive value of  $\alpha$  may arise due to the combined effect of poor resolution and free-free absorption by the plasma ejected during different episodes. We estimated the integrated spectral index to be  $-0.48 \pm 0.04$  by comparing the flux densities at 325 MHz (Rao et al. 2023) and 10 GHz. Additionally, we find that the kinetic jet power of the NGC 2639 is comparable to that of other Seyferts/LINERs and does not stand out as particularly special even though it produces multiple jet episodes.

#### 4.1.4. NGC 2992

NGC 2992 is changing-look (CL) Seyfert galaxy with extreme variability (Gilli et al. 2000; Marinucci et al. 2018; Ramos Almeida et al. 2009), hosting a nuclear ultra-fast outflow (UFO) with a velocity up to  $\sim 0.4c$  (Marinucci et al. 2018; Luminari et al. 2023). An 8-shaped AGN outflow almost perpendicular to the galac-

tic disc is detected at 5 GHz (Ulvestad & Wilson 1984). This galaxy is also part of a tidally interactive system along with three other galaxies, namely, NGC 2993, Arp 245, and dwarf A245 (Duc et al. 2000).

We observe a core-halo-like radio structure at 10 GHz with the VLA D-array. The H $\alpha$  image from the Continuum Halos in Nearby Galaxies - an EVLA Survey (CHANG-ES; Vargas et al. 2019) shows two components that may be due to the two rotating arms of the spiral host galaxy. Wehrle & Morris (1988) suggest that the prominent division in the H $\alpha$  map into two bulges might be due to obscuration by the dust lane along the disk of the galaxy. Alternately, the fainter component which coincides with the higher fractional polarization region ( $10.9 \pm 0.3\%$ ) with a steeper spectral index (see Figure 5, top panels & bottom left panel) might represent the relic lobe discovered in polarized light by Irwin et al. (2017). The H $\alpha$  emission is brightest in the nuclear region as seen in the VLA  $0.5''$  resolution image in Figure 5 (bottom right panel) and follows the spiral arms of the galaxy (Durret & Bergeron 1987; Wehrle & Morris 1988).

The 8-shaped lobed structure observed in the high-resolution VLA image (see Figure 5, bottom right panel) may result from bi-directional spherical shells of shocked gas or from magnetic loops/arches (Wehrle & Morris 1988). Xu et al. (2024) found an enhanced young stellar population at the boundary of the nuclear bubble, as well as an anti-correlation between AGN fraction and young stellar population up to 1 kpc from the nucleus, indicating low SFR in AGN outflow regions. These findings suggest that both positive and negative AGN feedback coexist in NGC 2992.

Our observations reveal more diffuse radio emission of extent  $39''$  ( $\sim 7$  kpc) compared to the  $\sim 1.5$  kpc long 8-shaped radio lobes. The polarization vectors show that the inferred B-fields are perpendicular to the direction of the 8-shaped Seyfert outflow. Given the outflow direction and a steep spectrum core (mean  $\alpha \approx -0.8 \pm 0.1$ ), the inferred B-fields are toroidal at the jet base. Toroidal B-fields are consistent with AGN winds along with the jets/lobes (Mehdipour & Costantini 2019). AGN-driven winds also have been suggested in this source by Zanchettin et al. (2023).

#### 4.1.5. NGC 3079

NGC 3079 is an edge-on barred spiral LINER + starburst composite galaxy (Heckman 1980; Irwin & Saikia 2003). The parsec-scale jet is found to be misaligned to the kpc-scale radio bubble by about  $65^\circ$  (Irwin & Seaquist 1988). Given the negligible projection effects (e.g., Readhead et al. 1983) for such an edge-on galaxy,

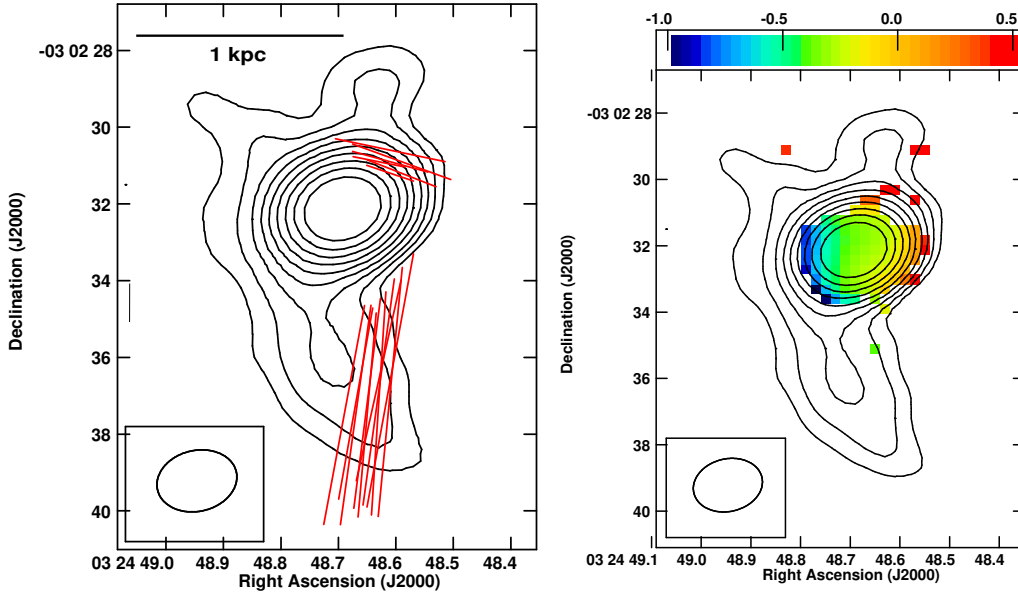


**Figure 3.** (Left) NGC 1320 image at 1.46 GHz with the VLA BnA→A array. For all the panels the contour levels are at  $3\sigma \times (-1, 1, 1.414, 2, 2.828, 4, 5.657, 8, 11.31, 16)$  with  $\sigma = 40 \mu\text{Jy beam}^{-1}$ . Similarly, the synthesized beam size is  $2.11'' \times 1.59''$  at a PA of  $-77.0^\circ$ . The tick lengths are proportional to fractional polarization;  $3'' = 1\%$ . Fractional polarization of errors  $> 35\%$  have been blanked. (Right) The VLA in-band spectral index image of NGC 1320. The spectral index values are in colour ranging from -1.0 to 0.5.

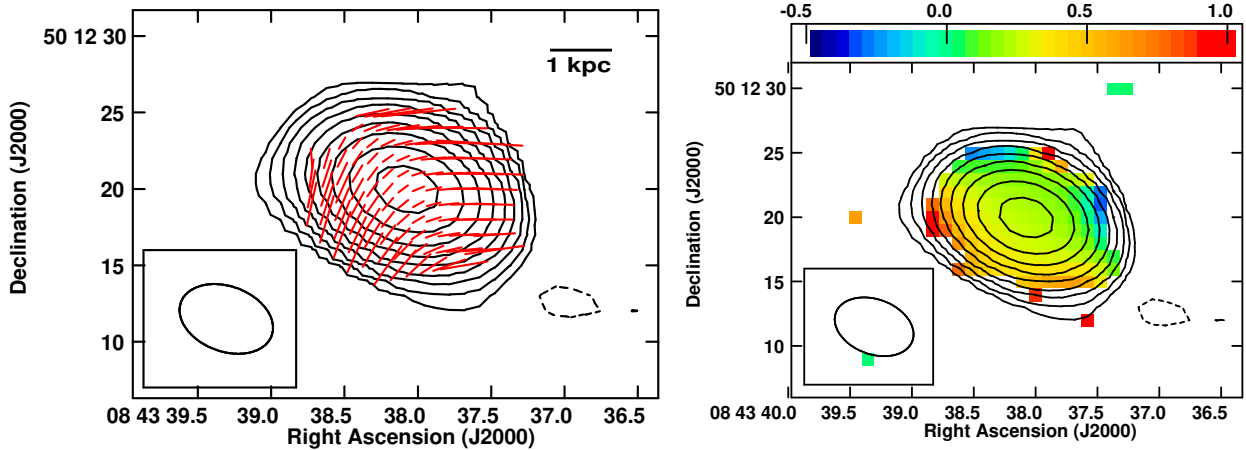


**Figure 4.** (Left) NGC 2639 image at 10 GHz with the VLA D-array. For all the panels the contour levels are at  $3\sigma \times (-0.4, 1, 2, 4, 8, 16, 32, 64, 128, 256)$  with  $\sigma = 15 \mu\text{Jy beam}^{-1}$ . Similarly, the synthesized beam size is  $6.33'' \times 4.26''$  at a PA of  $69.7^\circ$ . The tick lengths are proportional to fractional polarization;  $2'' = 2\%$ . (Right) In-band spectral index image of NGC 2639 centred at 10 GHz. The spectral index values are in colour ranging from -0.5 to 1.0.

such large misalignments are rarely observed except for new findings like NGC 2639 (for details, see Section 4.1.3). Although, the images at all scales put together construct an image of steady jet bending till the outflow manages to channel out along the minor axis (Irwin & Seaquist 1988). This idea is also supported by simulations, which find that highly inclined jets interact with the disc causing a wide outflow by drawing materials (gas clouds and filaments) from the disc and thereby affecting the ISM on kpc-scales then channelising its way

out along the minor axis of the host galaxy (Mukherjee et al. 2018).

Alternately, based on a VLBI study, Middelberg et al. (2007) suggested that the jet of NGC 3079 undergoes a strong interaction with the surrounding clumpy gas within a few parsec radius. The simulations by Saxton et al. (2005) show that this interaction causes the jet to form a large expanding radio bubble reaching kpc-scales, which explains the observed H $\alpha$  and X-ray superbubbles of size  $13''$  ( $\sim 1$  kpc) (Veilleux et al. 1994;

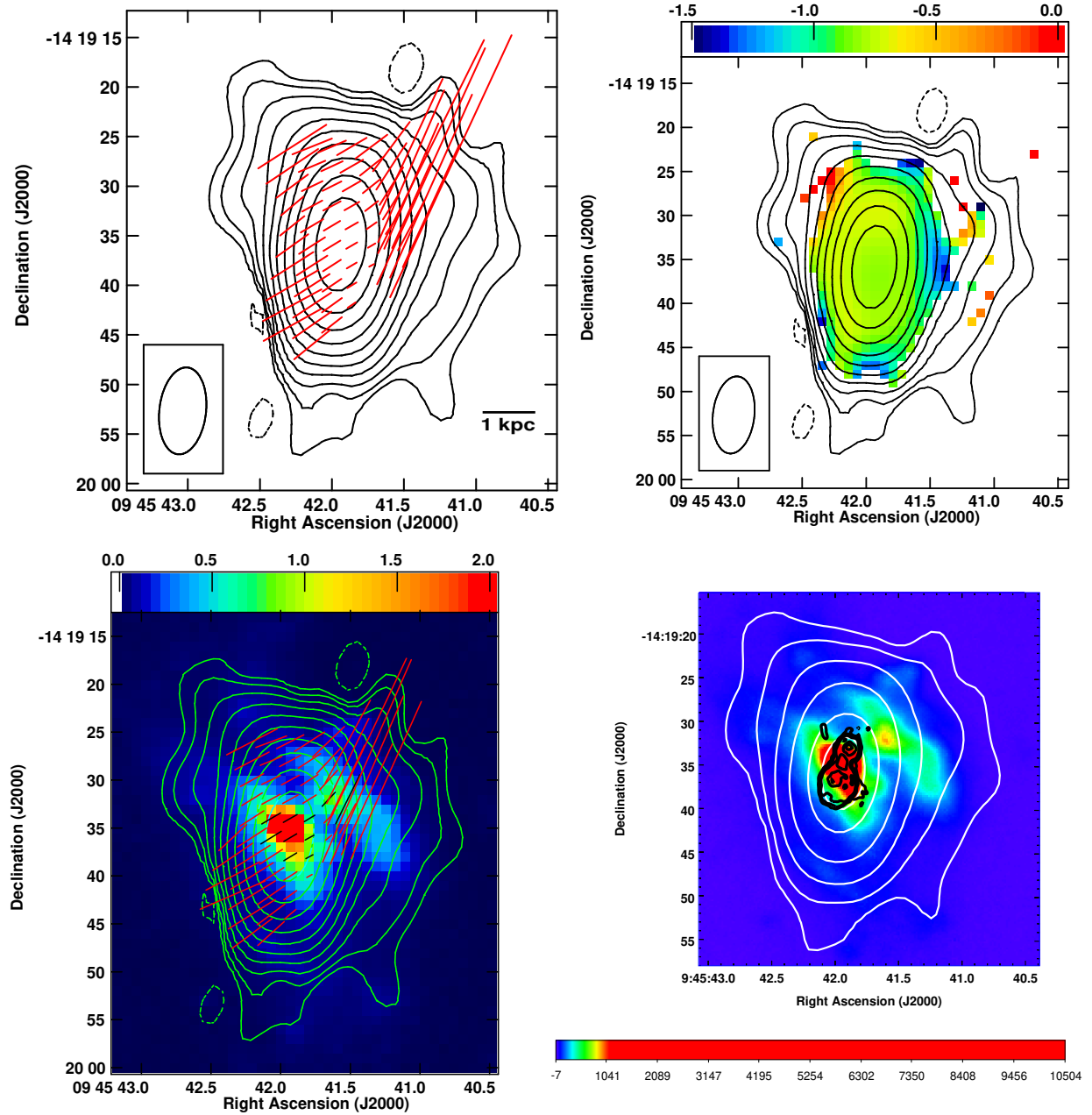


**Figure 5.** (Top left) Seyfert galaxy NGC 2992 image at 10 GHz with the VLA D array. For all the panels the contour levels are at  $3\sigma \times (-1, 1, 2, 4, 8, 16, 32, 64, 128, 256, 512)$  with  $\sigma = 12 \mu\text{Jy beam}^{-1}$ . Similarly, the synthesized beam size is  $8.81'' \times 4.71''$  at a PA of  $-6.5^\circ$ . The tick lengths are proportional to fractional polarization with  $5'' = 2.5\%$ . (Top right) In-band spectral index image of NGC 2992 centred at 10 GHz. The spectral index values are in colour ranging from  $-1.5$  to  $0$ . (Bottom left) Radio contours and polarization vectors from our work over-plotted on the H $\alpha$  image from the CHANG-ES survey for NGC 2992. The H $\alpha$  gas is in colour ranging from  $(0.0 \text{ to } 2000.0) \times 2.217 \times 10^{-19} \text{ erg s}^{-1} \text{ cm}^{-2}$ . The tick lengths are the same as the top left panel. (Bottom right) Radio contours over-plotted on the H $\alpha$  image from CHANG-ES. White contours are from our work. Black contours show an archival VLA 5 GHz image at a resolution of  $\sim 0.5''$  with contour levels at  $5\sigma \times (-1, 1, 2, 4, 8)$  with  $\sigma = 2 \mu\text{Jy beam}^{-1}$ .

Cecil et al. 2002). Strickland et al. (2004) argued that the H $\alpha$  and X-ray bubbles are unrelated to the 1.5 kpc radio jet and lobe, attributing their partial coincidence to projection effects. However, Li et al. (2024) has recently demonstrated that the energy injection required for maintaining pressure balance in the bubble cannot be explained solely by starburst activity but rather AGN activity is required. Unlike the H $\alpha$  gas that forms a superbubble in the nuclear region, the [OIII] gas is concentrated in compact regions along the galactic disk, peaking near the nucleus. These compact [OIII] emissions are thought to arise from photoionization by disk winds, with the brightest emission resulting from dust extinction near the nucleus (Robitaille et al. 2007).

From our work, radio emission is detected from the galactic disc extending about  $152''$  ( $\sim 14$  kpc) and the Seyfert outflow in a bipolar lobe, perpendicular to the galactic emission, extending about  $53''$  ( $\sim 5$  kpc). The radio emission is coincident with the H $\alpha$  image (CHANG-ES; Vargas et al. 2019), highlighting the synchrotron emission from the high star-forming regions (see Figure 6, bottom left panel). The core ( $f_p \approx 2\%$ ) and the lobe ( $f_p \approx 16\%$ ) stand out in polarization intensity compared to the galactic disk. The core is steep (mean  $\alpha = -0.9 \pm 0.2$ ), the lobe and the galactic disk are steeper and have similar mean spectral indices ( $\alpha = -1.5 \pm 0.2$ ) as in Figure 6 (top right panel). The inferred B-fields in the galactic plane (see Figure 6, top left panel, for the polarization vectors), are along the rotating disk.

The B-fields in the western lobe bend along the lobe’s curvature, indicating either confinement by the surrounding medium (e.g., Laing 1980a; Ghosh et al. 2023) or the presence of initially sheared B-field tangential to the surface without any outward component (Blandford & Rees 1978; Laing 1980b, 1981). In the Eastern lobe, the B-fields follow the bends initially but become perpendicular to the boundary at the edge of the radio bubble, differing from typical shocked regions (see also Cecil et al. 2001; Sebastian et al. 2019a). The inferred B-field at the core is aligned with the VLBI jet direction. The atomic neutral hydrogen (HI) map (CHANG-ES; Zheng et al. 2022) reveals a lack of neutral hydrogen along the Seyfert outflow (Figure 6; bottom right panel). This may suggest that AGN activity is depleting or ionizing the neutral gas. The presence of H $\alpha$  (Figure 6; bottom left panel) in the same region as the HI deficit supports this ionization hypothesis. The reduced amount of neutral gas, being the fuel reservoir for star formation, in the AGN outflow region, acts as a negative AGN feedback.

#### 4.1.6. NGC 3516

NGC 3516 is a barred lenticular galaxy hosting a CL AGN (Mehdipour et al. 2022). This galaxy is also identified as an ambiguous type 1 Seyfert (Gallimore et al. 2006a) with an S-shaped NLR which is more common to type 2s (see Fischer et al. 2013). The gradual weakening of the broad lines and their complete disappearance in 2014 has been noted by Shapovalova et al. (2019). Veilleux et al. (1993) have proposed two models for the S- or Z-shaped NLR: a precessing twin-jet model, where the precessing jet entrains NLR clouds, and a model where the gas-entraining jet is deflected by the ram pressure of the rotating spiral galaxy. In both scenarios, the radio jet interacts with the emission line gas, with the jet entraining the gas clouds rather than the gas ionizing the medium to produce synchrotron emission.

We observe the projected Seyfert outflow to be nearly aligned with the major axis of the host galaxy and extending up to  $\sim 54''$  ( $\sim 10$  kpc; Figure 7). We observe a flat-spectrum, depolarized core with a double-lobed structure in the north-east and south-west direction. After subtracting the core’s contribution, the approaching jet/lobe (see Miyaji et al. 1992; Mundell et al. 2009) is found to be three times brighter than the receding lobe, with flux densities of  $\sim 2.9$  mJy and  $\sim 0.96$  mJy, respectively. The inferred B-field structure observed in the north-east lobe is similar to that observed in a Fanaroff-Riley (FR) type II source; that is, the B-fields are aligned along the jet/outflow and become perpendicular in a hotspot-like region which also has a flatter spectral index. This is suggestive of a terminal shock that compresses B-fields and causes particle reacceleration.

#### 4.1.7. NGC 4051

NGC 4051 is a narrow-line Seyfert 1 (NLS1) inclined at an angle of  $12^\circ$  to our line of sight (Fischer et al. 2013; Khachikian & Weedman 1974). It has also been identified as a Seyfert type 1.5 (Gallimore et al. 2006a) hosted by a weakly barred spiral galaxy (Dumas et al. 2007). Similar to NGC 2992, this galaxy is known to harbour an UFO with velocity  $\sim 1.2c$  (Pounds & King 2013). The X-ray power spectrum shows similarity with the soft state of Cygnus X-1 and its low mass suggests a high accretion rate of about a few tens of per cent of the Eddington rate (Taylor et al. 2003). This source is found to be an analogue of a soft-state galactic black hole binary where jets are typically not found (Jones et al. 2011). However, VLBI observations reveal three compact regions in a line with an extension of  $\sim 1''$  ( $\sim 0.07$  kpc) at a PA of  $73^\circ$  at 1.5 GHz, confirming the existence of small-scale

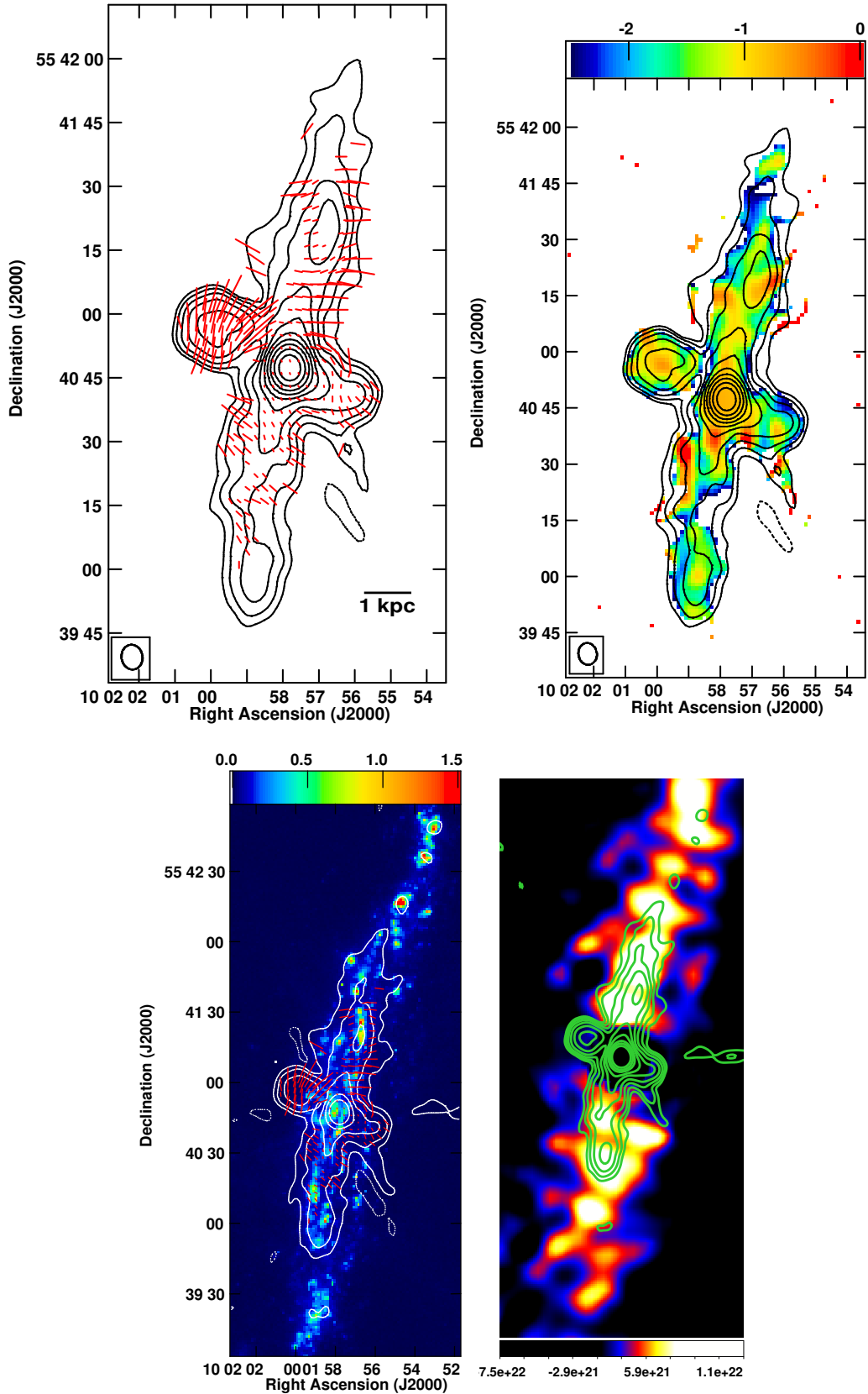


**Figure 6.** (Top left) NGC 3079 image at 10 GHz with the VLA D-array. Galactic radio emission is detected along with the KSR in this galaxy. For all the panels the contour levels are at  $3\sigma \times (-1, 1, 2, 4, 8, 16, 32, 64, 128, 256, 512)$  with  $\sigma = 50 \mu\text{Jy beam}^{-1}$ . Similarly, the synthesized beam size is  $5.86'' \times 4.93''$  at a PA of  $9.31^\circ$ . The tick lengths are proportional to fractional polarization with  $5'' = 25\%$ . (Top right) In-band spectral index image of NGC 3079 centred at 10 GHz. The spectral index values are in colour ranging from -2.5 to 0.0. (Bottom left) Radio contours with polarization vectors over-plotted on the H $\alpha$  image from CHANG-ES for the Seyfert galaxy NGC 3079. The H $\alpha$  is in colour ranging from  $(0.0 \text{ to } 1500.0) \times 2.086 \times 10^{-19} \text{ erg s}^{-1} \text{ cm}^{-2}$ . The tick lengths are the same as the top left panel. (Bottom right) Radio contours are overplotted on HI moment 0 map from CHANG-ES (Zheng et al. 2022).

jets in this source (Christopoulou et al. 1997; Giroletti & Panessa 2009; Jones et al. 2011).

At a resolution of  $\sim 7''$  ( $\sim 0.5$  kpc), we observe extended radio emission from this Seyfert galaxy with extent  $\sim 20''$  ( $\sim 1.3$  kpc) without resolving the core-jet structure. The spectral index image (Figure 8, right panel) shows that the ‘core’ is to the north of the peak radio emission, and a jet-core-jet structure is revealed by steep spectrum emission on either side of the flat spectrum core. Sebastian et al. (2020) reported a non-detection of polarization at 5 GHz with an upper limit of  $f_p = 14.3\%$ . We detect polarised emission from the northern lobe ( $f_p = 7 \pm 2\%$ , Figure 8, left panel), with B-fields aligned with the possible jet direction. No polarization is detected towards the south which could be due to the presence of a greater Faraday rotating medium to the south.

#### 4.1.8. NGC 4235

NGC 4235 is a nearly edge-on spiral galaxy without a bar hosting a Seyfert 1 nucleus (Abell et al. 1978; Jiménez-Benito et al. 2000; Gallimore et al. 2006a). The  $H\alpha + [NII]$ ,  $[OIII]\lambda 5007\text{\AA}$  emission lines are observed to have an extension along the major axis of the galaxy. No HII has been detected in the disk and no ionised gas has been detected above the galactic plane (Pogge 1989).

Our images show arc-like regions that are part of bubble-like lobes in the east-west direction, roughly perpendicular to the galactic disk (see also Colbert et al. 1996a). The maximum observed extent of the source is  $\sim 118''$  ( $\sim 22$  kpc). The western lobe (flux density  $\sim 0.9$  mJy) is brighter than the eastern lobe (flux density  $\sim 0.3$  mJy). Kharb et al. (2016) have found a bent jet-like feature connecting the core to the western lobe, which is consistent with the sub-arcsecond-scale image of Kukula et al. (1995) showing a north-west jet.

The eastern lobe emission is seen from behind the host galaxy disk (Colbert et al. 1996b; Malkan et al. 1998) which can explain the lack of significant polarization being due to the presence of greater Faraday rotating medium. Polarisation was not detected in this source at 5 GHz with an upper limit of 4.7% (Sebastian et al. 2020). At 10 GHz we detect polarization both in the core and the eastern and western lobes at the level of  $2.5 \pm 0.5\%$  and  $5 \pm 1\%$ , respectively. The inferred B-fields are aligned with the edges of the lobes (see Figure 9, top panel). Given the optically thick core ( $\alpha = +0.11 \pm 0.02$ ; Figure 9, bottom panel), the inferred B-fields are perpendicular to the sub-arcsec-scale jet direction.

#### 4.1.9. NGC 4388

NGC 4388 is an edge-on unbarred spiral galaxy near the Virgo cluster centre with a highly inclined disk to our

line of sight ( $\sim 78^\circ$ ), with the Northern part being closer to us (Phillips & Malin 1982; Chung et al. 2009). The galaxy is found to host a Seyfert type 2 nucleus (Phillips & Malin 1982). The radio emission from this source is found to be extra-planar, with high excitation gas like  $H\alpha + [NII]\lambda 6548$  and  $[OIII]\lambda 4959, \lambda 5007$  showing large extensions to the north-east, not exactly coinciding with the jet (Corbin et al. 1988; Veilleux et al. 2003). A tail of neutral hydrogen gas is observed away from the galaxy, leading to an HI deficiency in NGC 4388, supported by persistent ram-pressure stripping in the ICM (Vollmer & Huchtmeier 2003; Oosterloo & van Gorkom 2005). Studies indicate the presence of a precessing jet either due to a dual AGN or a precessing disk in this source (see Mueller Sanchez et al. 2022; Sargent et al. 2024).

The galactic emission with the Seyfert outflow along the minor axis of the galaxy is detected in our observations at 6 GHz and 10 GHz. The galactic disk exhibits a slightly steeper spectral index ( $\alpha \sim -1.2$ ) compared to the Seyfert outflow ( $\alpha \sim -0.8$ ; see Figures 10 and 11, middle panel). The Seyfert outflow also stands out in having higher fractional polarization, with  $f_p = 13 \pm 1\%$  at 10 GHz ( $5.6 \pm 0.8\%$  at 6 GHz), compared to the galactic disk’s  $f_p = 9 \pm 2\%$  at 10 GHz ( $4.1 \pm 0.7\%$  at 6 GHz; see Figures 10 and 11, top panel). The B-fields, assumed to be perpendicular to the EVPAs, are aligned along the galactic disk, with RM tracing the rotating disk. In contrast, the B-fields along the Seyfert lobe is observed to change directions over short scales ( $\sim 0.5$  kpc).

This rapid change in B-field directions observed may indicate jet wiggling caused by precession or strong jet-medium interactions. Stone et al. (1988) reported continuous bending of the radio emission along the length of the extra-planar ejecta from their multi-frequency radio observations. They attributed this to various processes such as gravitational pull, ram pressure bending by galactic gas or ICM, buoyancy maintenance due to the density gradient between the radio plasma and the surroundings, the presence of curved B-fields, and jet nozzle precession. From our observations, we conclude that either the curved B-field structures or the precessing jet nozzle model best explains the data.

The 10 GHz image detects no polarization at the core whereas the 6 GHz image detects a fractional polarization of  $\sim 1\%$  at the core. Figures 10 and 11 (bottom panel) show that the  $H\alpha$  gas (Vargas et al. 2019) is extended perpendicular to the disk but parallel to the B-field lines in the jet. The  $H\alpha$  emission is bright along the galaxy’s spiral arms. The 6 GHz image shows some radio-association with the  $H\alpha$  brightening and the jet. The  $H\alpha$  emission could be linked to young star formation activity driven by the radio jet. The lack of atomic

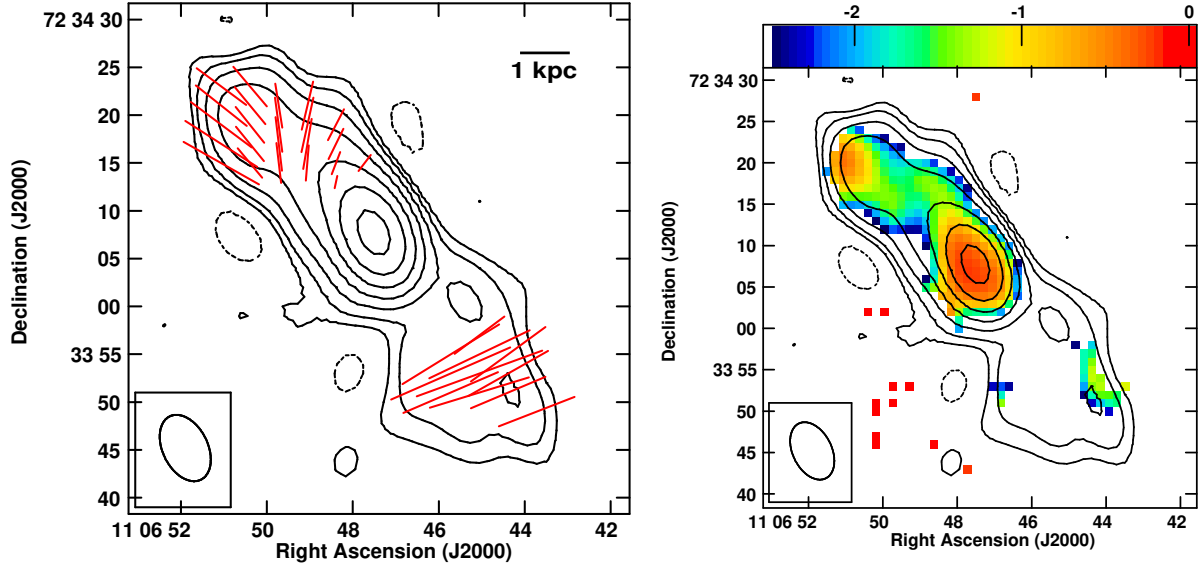


**Figure 7.** (Left) NGC 3516 at 10 GHz with the VLA D-array. For all the panels the contour levels are at  $3\sigma \times (-1, 1, 2, 4, 8, 16, 32, 64)$  with  $\sigma = 16 \mu\text{Jy beam}^{-1}$ . The synthesized beam size is  $7.38'' \times 4.71''$  at a PA of  $26.29^\circ$ . The tick lengths are proportional to fractional polarization with  $5'' = 12.5\%$ . (Right) In-band spectral index image of NGC 3516 centred at 10 GHz. The spectral index values are in colour ranging from -2.5 to 0.0.

hydrogen near the radio jet could be explained by excess star formation in that region, suggesting positive AGN feedback.

The RM image from CHANG-ES (Krause et al. 2020) shows an increase in RM at the core, where the linear polarization intensity drops and becomes depolarized at 10 GHz. Our preliminary analysis also detects low circular polarization (circularly polarized flux density of  $\sim 0.12 \text{ mJy}$ ) at the core of this source at 6 GHz. We obtain a maximum circular fractional polarization of 0.4% at the core at 6 GHz ( $> 0.3\%$  is considered a strong signal; Homan & Lister 2006). The region of circular polarization is coincident with the region lacking linear polarization. This might indicate Faraday conversion happening at the core of this source. Irwin et al. (2018) have recently found a circularly polarized structure in this source at 1.4 GHz. The detection of circular polarization in this source makes it interesting as it might be intrinsic to the source (i.e., not due to Faraday conversion) and could help in the determination of B-field strengths unambiguously and obtain limits on cosmic ray electron energies.

#### 4.1.10. NGC 4593

NGC 4593 is a barred spiral galaxy with outer and inner rings and a nuclear dust ring hosting a Seyfert 1 nucleus (Balzano 1983; Kollatschny & Fricke 1985) exhibiting extreme variability, especially in UV and X-ray spectra (Clavel et al. 1983; Santos-Lleo et al. 1995). NGC 4593 is thought to possess one of the smallest BLR known (Dietrich et al. 1994). Compared to the high-

resolution images of this source which showed a compact feature in radio (Schmitt et al. 2001), Gallimore et al. (2006a) found a lobed structure of extent of  $\sim 5 \text{ kpc}$  in this source.

Our observations show a weak extension in the radio emission of  $\sim 26''$  ( $\sim 5 \text{ kpc}$ ) in the east-west direction. Polarization with an inferred B-field aligned with the radio extension is observed in a region to the east of the core (see Figure 12; left panel). A spectral index steepening is observed in the same direction (Figure 12, right panel), more prominently towards the north-east and less prominently towards the north-west. These results are consistent with a small nearly east-west oriented double-lobed structure present in NGC 4593 in the 5 GHz image of Gallimore et al. (2006a). This structure is not resolved in our image but is reflected in the spectral index image suggesting the presence of a jet or lobe in the east-west direction. However, an inversion in the spectrum observed in the southern part of the source remains unexplained. The  $[\text{OIII}]\lambda 5007$  emission (Schmitt et al. 2003) coincides with the extended structure, with stronger emission on the west than the east of the core. The lack of polarization detection in the eastern lobe could be a consequence of a greater Faraday rotating medium (cold gas) in that direction.

#### 4.1.11. NGC 4594

NGC 4594 a.k.a. the Sombrero galaxy is an unbarred, edge-on, spiral galaxy with a large stellar bulge and a containing LINER type 2 nucleus (Heckman 1980; Giovanelli et al. 1986; Irwin et al. 2012). This galaxy is

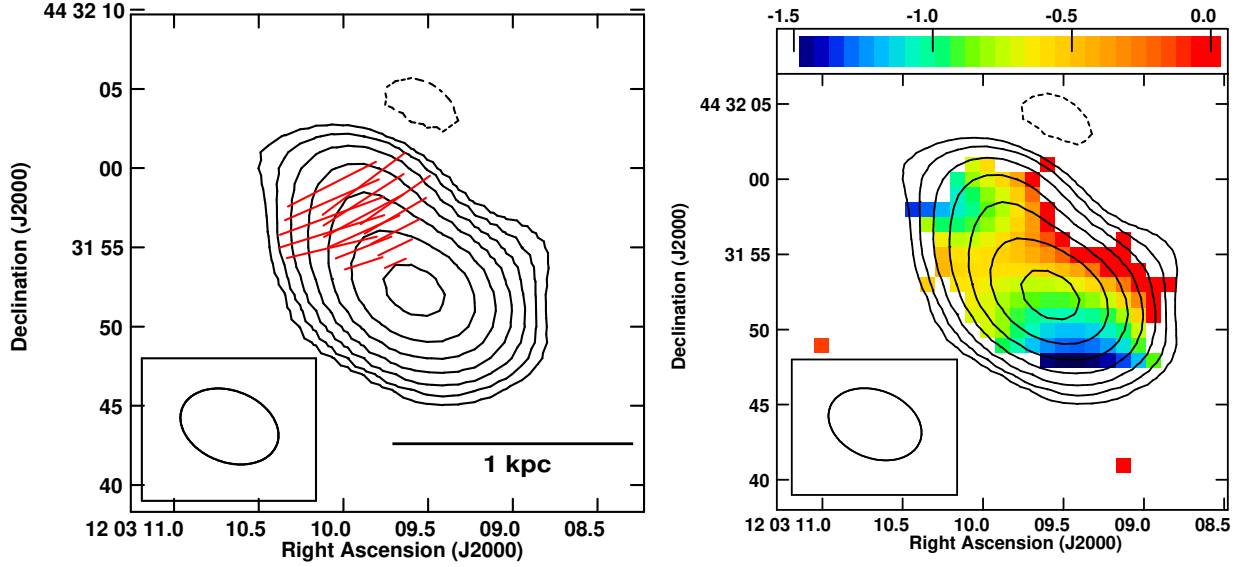


**Figure 8.** (Left) NGC 4051 image at 10 GHz with the VLA D array. For all the panels the contour levels are at  $3\sigma \times (-1, 1, 2, 4, 8, 16, 32, 64)$  with  $\sigma = 15 \mu\text{Jy beam}^{-1}$ . Similarly, the synthesized beam size is  $6.40'' \times 4.51''$  at a PA of  $69^\circ$ . The tick lengths are proportional to fractional polarization with  $2'' = 2.5\%$ . (Right) In-band spectral index image of NGC 4051 centered at 10 GHz. The spectral index values are in colour ranging from  $-1.5$  to  $0.0$ .

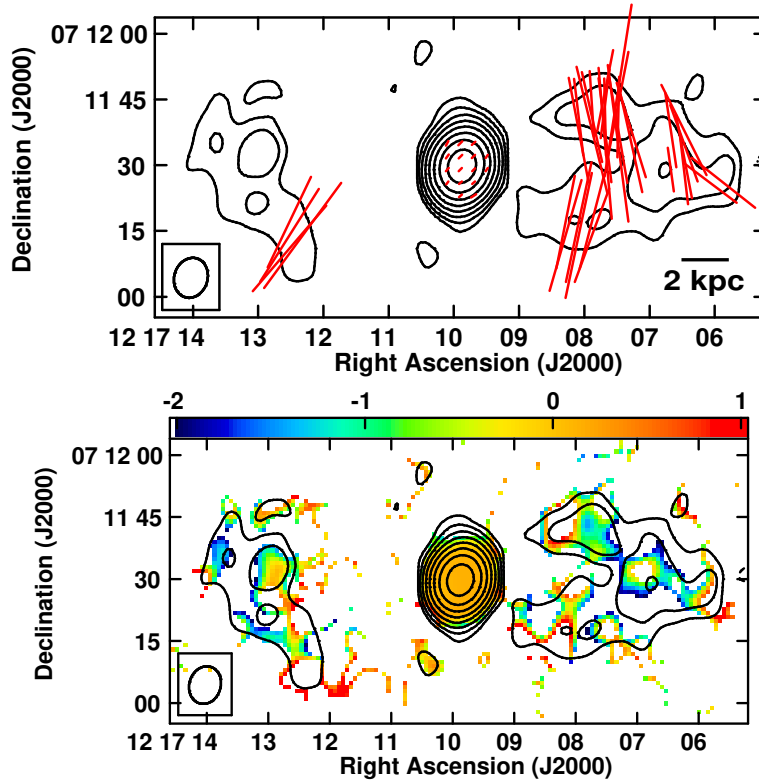


**Figure 9.** (Top) NGC 4235 image at 10 GHz with the VLA D array. For all the panels the contour levels are at  $3\sigma \times (-1, 1, 2, 4, 8, 16, 32, 64, 128)$  with  $\sigma = 10 \mu\text{Jy beam}^{-1}$ . Similarly, the synthesized beam size is  $9.24'' \times 7.60''$  at a PA of  $-17.18^\circ$ . The tick lengths are proportional to fractional polarization;  $10'' = 25\%$ . Fractional polarization of errors  $> 30\%$  have been blanked. (Bottom) In-band spectral index image of NGC 4235. The spectral index values are in colour ranging from  $-2.0$  to  $1.0$ .

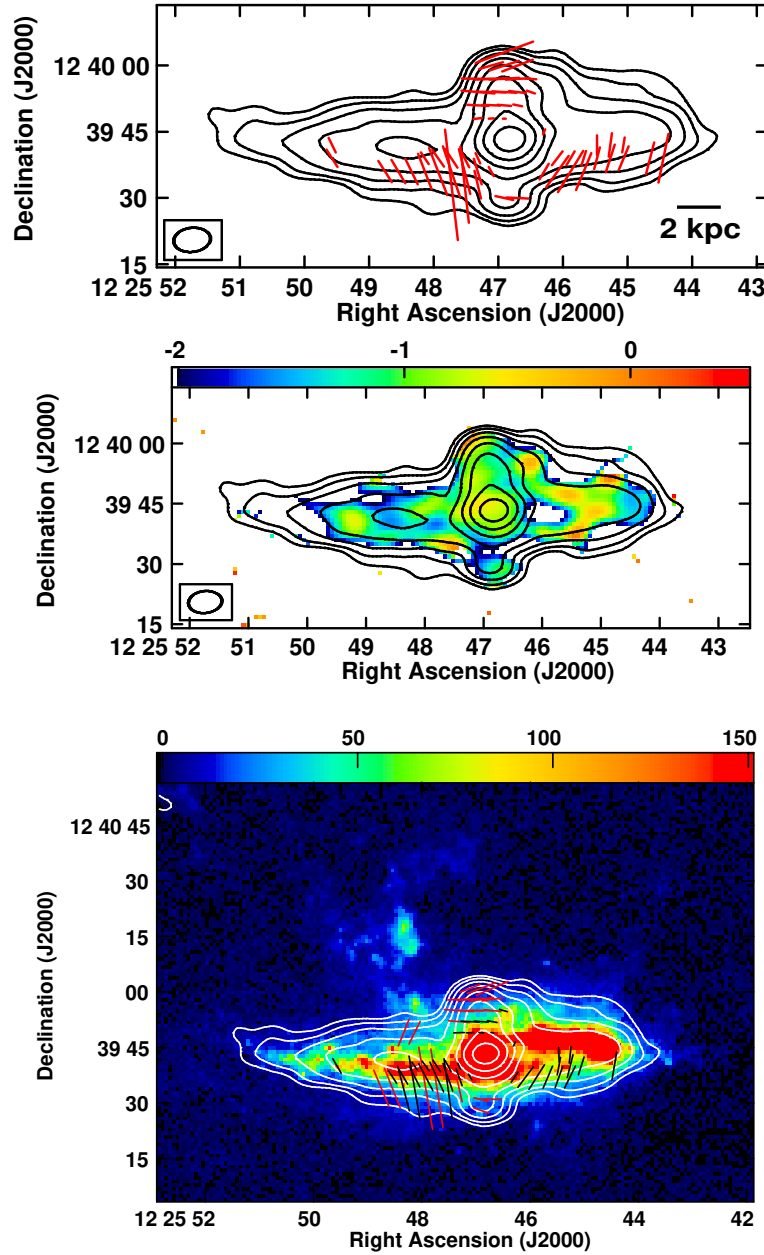


**Figure 10.** (Top) NGC 4388 image at 10 GHz with the VLA D array. Galactic radio emission is detected along with the KSR in this galaxy. For all the panels the contour levels are at  $3\sigma \times (-1, 1, 2, 4, 8, 16, 32, 64, 128)$  with  $\sigma = 20 \mu\text{Jy beam}^{-1}$ . Similarly, the synthesized beam size is  $8.36'' \times 5.47''$  at a PA of  $-83.7^\circ$ . The tick lengths are proportional to fractional polarization with  $10'' = 25\%$ . (Middle) In-band spectral index image of NGC 4388 centred at 10 GHz. The spectral index values in colour range from  $-2.0$  to  $+0.5$ . (Bottom) Radio contours and polarization vectors at 10 GHz overlapped on H $\alpha$  image from CHANG-ES. The H $\alpha$  is in colour ranging from  $(0.0 \text{ to } 150.0) \times 2.145 \times 10^{19} \text{ erg s}^{-1} \text{ cm}^{-1}$ . The tick lengths are the same as the top panel.

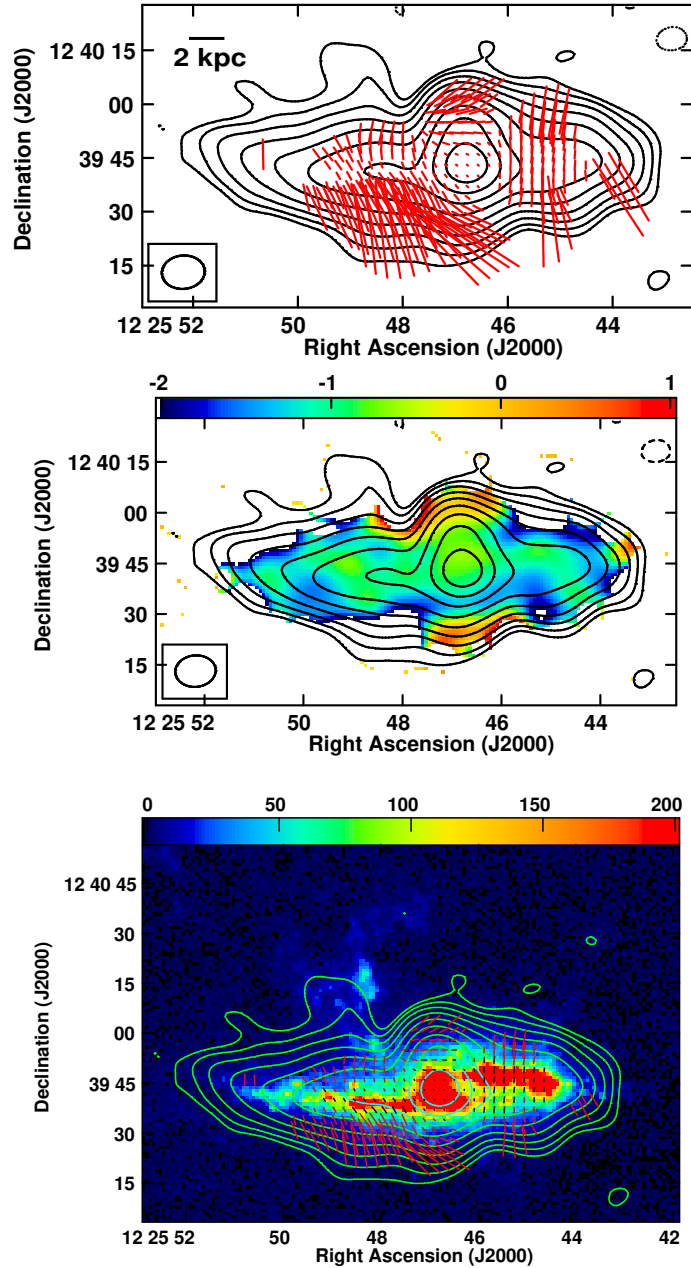


**Figure 11.** (Top) NGC 4388 image at 5.3 GHz with the VLA D array. *Galactic radio emission is detected along with the KSR in this galaxy.* For all the panels the contour levels are at  $3\sigma \times (-1, 1, 2, 4, 8, 16, 32, 64, 128, 256)$  with  $\sigma = 17 \mu\text{Jy beam}^{-1}$ . Similarly, the synthesized beam size is  $11.99'' \times 9.31''$  at a PA of  $-85.0^\circ$ . The tick lengths are proportional to fractional polarization with  $10'' = 10\%$ . (Middle) In-band spectral index image of NGC 4388 at C-band. The spectral index values are in colour ranging from -2.0 to 1.0. (Bottom) Radio contours and polarization vectors at C-band over-plotted on the  $\text{H}\alpha$  image from CHANG-ES. The  $\text{H}\alpha$  is in colour ranging from  $(0.0 \text{ to } 200.0) \times 2.145 \times 10^{19} \text{ erg s}^{-1} \text{ cm}^{-2}$ . The tick lengths are proportional to fractional polarization with  $10'' = 25\%$ .

**Table 3.** Summary of the Polarization Properties.

Source	Frequency	Region	$I_P$ (mJy)	FP (%)	$\chi$ (degrees)
NGC 1068	1.4 GHz	Core	$3.0 \pm 0.7$	$0.51 \pm 0.01$	...
		Northern lobe	$5.7 \pm 0.2$	$3.9 \pm 0.4$	$7 \pm 2$
		Southern lobe	$1.9 \pm 0.1$	$0.9 \pm 0.04$	$-28 \pm 2$
		East polarized region	$0.8 \pm 0.1$	$3.2 \pm 0.4$	...
		Total	$24 \pm 1$	$1.7 \pm 0.3$	...
NGC 1320	1.4 GHz	Core	$5 \times 10^{-3}(\text{u})$	0.73(u)	...
		North-west lobe	$0.019 \pm 0.006$	$20 \pm 6$	$72 \pm 9$
		Southern lobe	$0.030 \pm 0.009$	$47 \pm 18$	$-8 \pm 9$
		Total	$0.05 \pm 0.01$	$36 \pm 13$	...
NGC 2639	10 GHz	Core	$0.37 \pm 0.01$	$1.2 \pm 0.4$	$-35 \pm 3$
		Total	$0.72 \pm 0.04$	$2.2 \pm 0.2$	...
NGC 2992	10 GHz	Core	$0.20 \pm 0.05$	$1.0 \pm 0.4$	$-53 \pm 4$
		Total	$0.51 \pm 0.05$	$2.9 \pm 0.6$	...
NGC 3079	10 GHz	Core	$2.0 \pm 0.1$	$2.2 \pm 0.1$	$28 \pm 2$
		East-West lobe	$7.3 \pm 0.2$	$16 \pm 2$	...
		Galactic disk	$0.9 \pm 0.2$	$12 \pm 2$	$7 \pm 6$
		Total	$7.3 \pm 0.3$	$14.4 \pm 1.2$	...
NGC 3516	10 GHz	Core	$27 \times 10^{-4}(\text{u})$	0.06(u)	...
		Extended lobe	$0.28 \pm 0.05$	$17 \pm 4$	...
		Total	$0.27 \pm 0.05$	$17 \pm 0.4$	...
NGC 4051	10 GHz	Core	$3.9 \times 10^{-3}(\text{u})$	0.32(u)	...
		Extended lobe	$0.06 \pm 0.01$	$7 \pm 2$	$-66 \pm 7$
		Total	$0.06 \pm 0.01$	$6.3 \pm 1.8$	...
NGC 4235	10 GHz	Core	$0.13 \pm 0.02$	$2.5 \pm 0.5$	$-42 \pm 5$
		Western lobe	$0.39 \pm 0.08$	$5 \pm 1$	...
		Eastern lobe	$0.23 \pm 0.01$	$2.5 \pm 0.5$	...
		Total	$0.37 \pm 0.08$	$5 \pm 1$	...
NGC 4388	10 GHz	Core	$6 \times 10^{-3}(\text{u})$	0.04(u)	...
		Northern lobe	$0.81 \pm 0.09$	$13 \pm 1$	...
		Galactic disk	$0.25 \pm 0.05$	$9 \pm 2$	$\pm 18 \pm 7$
		Total	$0.72 \pm 0.07$	$12.3 \pm 1.7$	...
NGC 4593	10 GHz	Core	$12 \times 10^{-3}(\text{u})$	0.5(u)	...
		Extended lobe	$0.07 \pm 0.02$	$16.9 \pm 0.5$	$-26 \pm 8$
		Total	$0.08 \pm 0.02$	$16.9 \pm 0.5$	...
NGC 4594	10 GHz	Core	$0.50 \pm 0.06$	$0.6 \pm 0.3$	$54 \pm 3$
		Total	$0.71 \pm 0.02$	$0.9 \pm 0.1$	...
NGC 5506	10 GHz	Core	$0.05 \pm 0.01$	$0.10 \pm 0.02$	$-28 \pm 7$
		Total	$0.12 \pm 0.03$	$5 \pm 1$	...

Column 1: Name of the sources. Column 2: Observing frequency. Column 3: Source region selected for analysis. Column 4: Mean polarized intensity in that region in mJy. Column 5: Mean polarization fraction in that region in %. Column 6: Mean angle of the polarized vectors in degrees in that region. Sources with polarized intensity and polarization fraction values but not with polarization angle values presented here imply that the vectors are oriented at multiple angles within the selected region. (u) denotes an upper limit.

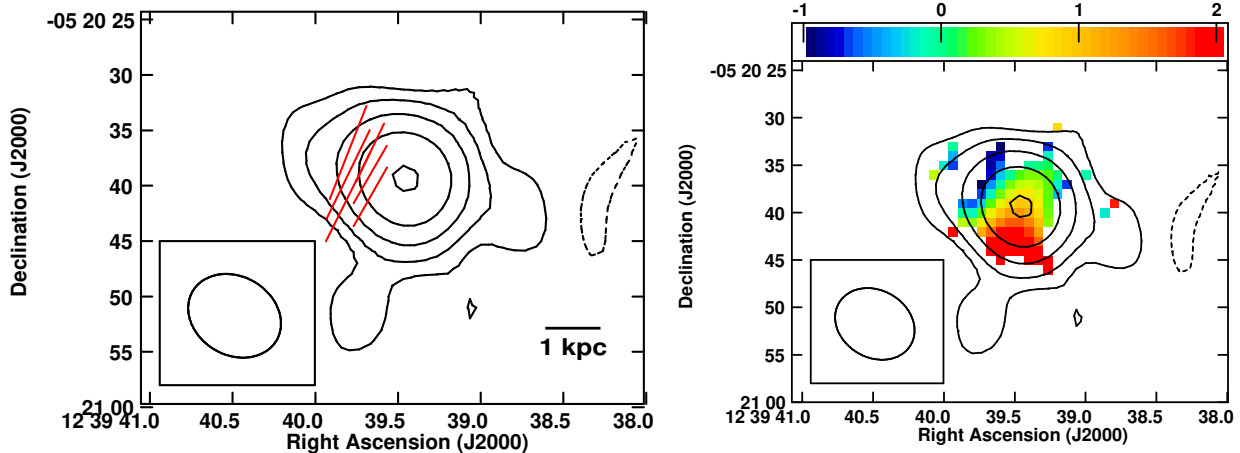


**Figure 12.** (Top) NGC 4593 image at 10 GHz with the VLA D array. For all the panels the contour levels are at  $3\sigma \times (-1, 1, 2, 4, 8, 16)$  with  $\sigma = 45 \mu\text{Jy beam}^{-1}$ . Similarly, the synthesized beam size is  $8.77'' \times 7.09''$  at a PA of  $59.74^\circ$ . The ticks are proportional to fractional polarization;  $5'' = 12.5\%$ . (Bottom) In-band spectral index image of NGC 4593 centred at 10 GHz. The spectral index values are in colour ranging from  $-1.0$  to  $+2.0$ .

found to be a poorly star-forming galaxy in comparison to other galaxies of similar type, although dominated by Type 1a supernovae activity in the ISM (Li et al. 2011, 2016; Jiang et al. 2024). Jiang et al. (2024) suggested that this galaxy might have gone through a starburst stage at an earlier time, and has now become a quiescent one. The accretion flow in this source partially resolvable by the Event Horizon Telescope (EHT; Bandyopadhyay et al. 2019).

Gallimore et al. (2006a) observed faint radio emission (highly polarised; Bajaja et al. 1988) obliquely oriented along the galactic minor axis which is suggested to be arising from the weak KSR. Our sensitive observations also show a stretch of radio emission along the galactic plane similar to that observed by Kharb et al. (2016); Yang et al. (2024), which is supposedly coming due to synchrotron emission from the previous supernova activity. The Seyfert emission lies perpendicular to the galactic disk. We detect a flat spectrum ( $-0.13 \pm 0.06$ ) core of  $112 \pm 6$  Jy consistent with the findings by Hummel et al. (1984). In Figure 13 (bottom panel), the steepening of the spectrum towards the north probably indicates the presence of an outflow in that direction. The core is polarized and the B-field directions are oblique to the extended outflow (see Figure 13; top panel). A sub-parsec-scale jet (brighter towards the north) is observed (Hada et al. 2013; Mezcuca & Prieto 2014) in an oblique direction, perpendicular to our inferred B-field direction, suggesting that the B-fields are toroidal in the jet.

#### 4.1.12. NGC 5506

NGC 5506 is an edge-on spiral galaxy hosting a Seyfert nucleus. The nucleus was initially identified as a Seyfert

type 2 by Rubin (1978) but later classified as an NLS1 by Nagar et al. (2002b) and as a Seyfert 1.9 by Gallimore et al. (2006a); Fischer et al. (2013).

Our observations of NGC 5506 show a diffuse radio halo surrounding the core. It shows very faint polarized structures ( $f_p = 0.5 \pm 0.1\%$ ) away from the central region. The directions of the EVPAs as shown in Figure 14 (left panel) appear to vary across different regions and appear to rotate around the core's circumference, indicating a complex polarized structure, as also observed by Sebastian et al. (2020). This complexity may result from multiple individual components within the unresolved core. The inferred B-field orientation in an ordered radial pattern could suggest jet precession, varying jet orientations at different scales, or a toroidal B-field at the jet base.

The spectral index image (see Figure 14; right panel) does not reveal any particular directionality of the outflow, rather the absence of a flat core signifies the presence of unresolved outflow at this resolution. Our observations reveal extended emissions towards the south, also marked by a higher degree of polarization ( $f_p = 19 \pm 5\%$ ) and a spectral flattening (disregarding the edge pixels  $\alpha \sim -0.2$ ) at its base. It is interesting to note that this southern extension is also observed in the  $[\text{OIII}]\lambda 5007$  image presented by Esposito et al. (2024) which is suggested to be arising due to the biconical outflow as observed in NLRs.

#### 4.2. Jet Powers

The power transported by the radio jets in Seyferts and LINERs, either kinetically or radiatively, can provide us a measure of the power ejected by the central engine. It is expected that radio core emission and the

**Table 4.** Jet power estimates

Source name	$L_{\text{core},10\text{GHz}}$ ( $10^{28}$ W Hz $^{-1}$ sr $^{-1}$ )	$\alpha_C$	$\log P_{\text{jet,rad}}$ (erg s $^{-1}$ ) (Foschini 2014)	$\log P_{\text{jet,kin}}$ (erg s $^{-1}$ ) (Merloni & Fabian 2002)
NGC 1068	0.35	$-0.371 \pm 0.04$	$40 \pm 3$	$43 \pm 6$
NGC 1320	9.46	$-0.808 \pm 0.001$	$41 \pm 3$	$42 \pm 6$
NGC 2639	15.51	$0.247 \pm 0.003$	$42 \pm 3$	$43 \pm 6$
NGC 2992	4.81	$-0.773 \pm 0.006$	$41 \pm 3$	$43 \pm 6$
NGC 3079	4.88	$-0.821 \pm 0.002$	$41 \pm 3$	$43 \pm 6$
NGC 3516	0.74	$-0.44 \pm 0.03$	$41 \pm 3$	$42 \pm 6$
NGC 4051	0.05	$-0.80 \pm 0.04$	$40 \pm 3$	$41 \pm 6$
NGC 4235	0.82	$0.11 \pm 0.02$	$41 \pm 3$	$42 \pm 6$
NGC 4388	1.96	$-0.78 \pm 0.01$	$41 \pm 3$	$43 \pm 6$
NGC 4593	0.372	$0.70 \pm 0.05$	$40 \pm 3$	$42 \pm 6$
NGC 4594	3.48	$-0.128 \pm 0.005$	$41 \pm 3$	$43 \pm 6$
NGC 5506	9.06	$-0.9 \pm 0.2$	$41 \pm 3$	$43 \pm 6$

Column 1: Names of the sources. Column 2: Core luminosity in the units of  $10^{28}$  erg s $^{-1}$  Hz $^{-1}$  Sr $^{-1}$  at 10 GHz using  $4\pi D_L^2 S_{\text{peak},10\text{GHz}} / (1+z)^{1+\alpha_C}$ , where  $S_{\text{peak},10\text{GHz}}$  is the peak brightness in units of mJy beam $^{-1}$  with a beam area of 1 unit. Column 3: Average in-band spectral index evaluated at the core (highest one or two contour levels). Column 4: Logarithm of jet radiative power in erg s $^{-1}$  using relations from Foschini (2014). Column 5: Logarithm of jet kinetic power in erg s $^{-1}$  using relations from Merloni & Heinz (2007).

**Table 5.** Summary of the Energetics

Source name	$\alpha$ (in-band)	$S_C$ (mJy)	$L_{\text{rad}}$ ( $10^{38}$ erg s $^{-1}$ )	$B_{\text{min}}$ ( $10^{-6}$ G)	$E_{\text{total}}$ ( $10^{54}$ ergs)	$\tau$ ( $10^7$ yr)
NGC 1068	$-0.85 \pm 0.01$	$365 \pm 18$	$40 \pm 2$	$63 \pm 7$	$1.3 \pm 0.2$	$0.052 \pm 0.009$
NGC 1320	$-0.37 \pm 0.04$	$1.9 \pm 0.1$	$0.76 \pm 0.06$	$6.2 \pm 0.6$	$0.38 \pm 0.05$	$1.2 \pm 0.1$
NGC 2639	$0.28 \pm 0.09$	$54 \pm 3$	$21 \pm 1$	$5.4 \pm 0.3$	$4.3 \pm 0.4$	$1.31 \pm 0.05$
NGC 2992	$-0.78 \pm 0.01$	$42.0 \pm 2.1$	$19 \pm 1$	$8.5 \pm 0.4$	$12.4 \pm 0.8$	$0.86 \pm 0.04$
NGC 3079	$-0.9 \pm 0.2$	$172 \pm 9$	$23 \pm 1$	$33 \pm 3$	$2.4 \pm 0.3$	$0.14 \pm 0.02$
NGC 3516	$-0.66 \pm 0.04$	$3.5 \pm 0.2$	$1.8 \pm 0.1$	$7.1 \pm 0.6$	$1.2 \pm 0.1$	$1.02 \pm 0.08$
NGC 4051	$-0.73 \pm 0.07$	$5.2 \pm 0.2$	$0.23 \pm 0.02$	$13 \pm 1$	$0.08 \pm 0.01$	$0.52 \pm 0.07$
NGC 4235	$-0.03 \pm 0.1$	$6.3 \pm 0.3$	$1.3 \pm 0.1$	$2.7 \pm 0.1$	$1.5 \pm 0.1$	$1.793 \pm 0.007$
NGC 4388	$-0.88 \pm 0.02$	$15.5 \pm 0.8$	$9.4 \pm 0.6$	$11.6 \pm 0.9$	$4.5 \pm 0.5$	$6.2 \pm 0.6$
NGC 4593	$0.5 \pm 0.2$	$2.5 \pm 0.2$	$0.51 \pm 0.04$	$1.62 \pm 0.08$	$0.32 \pm 0.03$	$1.75 \pm 0.02$
NGC 4594	$-0.13 \pm 0.06$	$112 \pm 6$	$5.6 \pm 0.4$	$6.7 \pm 0.3$	$1.9 \pm 0.1$	$1.10 \pm 0.04$
NGC 5506	$-0.9 \pm 0.2$	$108 \pm 5$	$38 \pm 15$	$15 \pm 2$	$14 \pm 3$	$0.4 \pm 0.07$

Column 1: Names of the sources. For the following columns estimates have been obtained for the core and surrounding diffuse emission excluding the extended jets/lobes. Column 2: In-band spectral index from either VLA 8 – 12 GHz or 1 – 2 GHz VLA data. Column 3: Flux density in mJy at 10 GHz. Column 4: Radio luminosity in unit of  $10^{38}$  erg s $^{-1}$  using  $S_C$  and  $\alpha$ . Column 5: Magnetic field value in the  $\mu$ G at minimum pressure under equipartition condition. Column 6: Total energy in units of  $10^{54}$  erg, including particle energy and field energy, at minimum energy. Column 7: Electron lifetimes in the units of 10 Myr due to synchrotron and IC CMB losses.

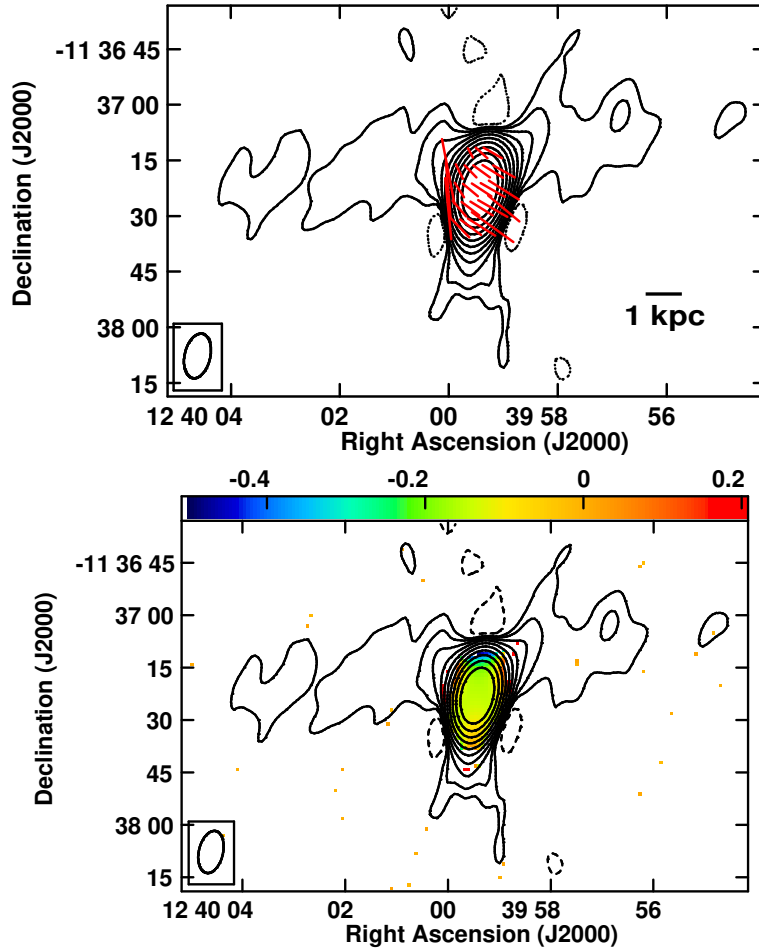


**Figure 13.** (Top) NGC 4594 image at 10 GHz with the VLA D array. Galactic radio emission is detected along with the KSR in this galaxy. For all the panels the contour levels are at  $3\sigma \times (-1, 1, 2, 4, 8, 16, 32, 64, 128, 256, 512)$  with  $\sigma = 22 \mu\text{Jy beam}^{-1}$ . Similarly, the synthesized beam size is  $12.26'' \times 6.90''$  at a PA of  $-12.96^\circ$ . The ticks are proportional to fractional polarization;  $10'' = 1\%$ . (Bottom) The VLA in-band spectral index image of NGC 4594. The spectral index values are in colour ranging from  $-1.5$  to  $+0.2$ .

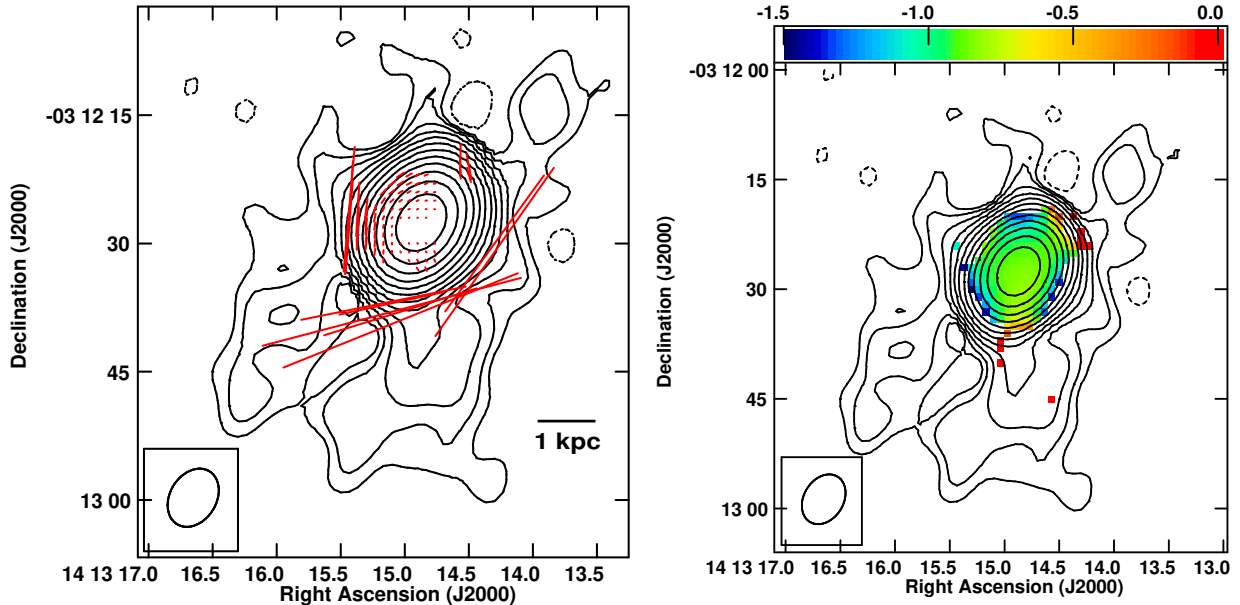


**Figure 14.** (Left) NGC 5506 image at 10 GHz with the VLA D array. For all the panels the contour levels are at  $3\sigma \times (-1, 1, 2, 4, 8, 16, 32, 64, 128, 256, 512, 1024, 2048)$  with  $\sigma = 9 \mu\text{Jy beam}^{-1}$ . Similarly, the synthesized beam size is  $7.25'' \times 5.42''$  at a PA of  $-31.47^\circ$ . The tick lengths are proportional to fractional polarization;  $5'' = 2.5\%$ . (Right) In-band spectral index image of NGC 5506 centred at 10 GHz. The spectral index values are in colour ranging from  $-1.5$  to  $0$ .

kpc-scale jet kinetic power must be correlated since both arise from the jets (Punsly 2005; Merloni & Heinz 2007; Cavagnolo et al. 2010). Therefore, the radio luminosity of the core becomes an important tool to probe the energy transported from the AGN to the jet as it propagates in the surrounding medium. Theoretical models for AGN with conical jets predict that the radio luminosity of the flat-spectrum optically thick radio core emission depends on the jet power as  $L_{\text{core}} \propto P_{\text{jet}}^{17/12}$  (Blandford & Königl 1979; Heinz & Sunyaev 2003). Later, observational measurements gave best-suited empirical relations between the core radio luminosity and jet power. Foschini (2014) found a correlation between the observed core radio power and the jet power obtained from spectral energy distribution (SED) modeling by Ghisellini & Tavecchio (2009):

$$\log P_{\text{jet,rad}} = (0.75 \pm 0.04) \log(\nu L_{\text{core},15\text{GHz}}) + (12 \pm 2) \quad (1)$$

$$\log P_{\text{jet,kin}} = (0.90 \pm 0.04) \log(\nu L_{\text{core},15\text{GHz}}) + (6 \pm 2) \quad (2)$$

where,  $P_{\text{jet,rad}}$  is the radiative jet power,  $P_{\text{jet,kin}}$  is the kinetic (electrons, protons, and B-field) jet power, and  $L_{\text{core},15\text{GHz}}$  the radio core luminosity at 15 GHz. Though the coefficient does not entirely match the theoretical value, the values are within  $2\sigma$  of each other. The  $L_{\text{core},15\text{GHz}}$  is calculated from 10 GHz core (peak) flux ( $S_{\text{peak}}$ ) as  $L_{\text{core},\nu} = 4\pi D_L^2 S_{\text{peak},\nu} / (1+z)^{1+\alpha}$ , and  $S_{\text{peak},\nu} = (\nu/10)^{\alpha_c} \times S_{\text{peak}}$ , considering K-correction,  $\nu$  as 15 GHz, and  $\alpha$  as the spectral index at the core. These relations have been derived for high-resolution

(mostly VLBI) data but have also been applied for single dish observations (e.g., Angelakis et al. 2015). Typically only a fraction of the flux densities at VLA scales can be recovered at VLBI scales (see Orienti & Prieto 2010; Kharb et al. 2021). Since our estimates are based on VLA core flux densities, the jet powers estimated here could be an overestimate. Following the equations 1 and 2, the derived values of  $\log P_{\text{jet,rad}}$ ,  $\log P_{\text{jet,kin}}$  have been tabulated in Table 4.

Since none of these relations were estimated for low-luminosity radio-quiet AGN like Seyferts and LINERs, we calculated the jet powers using other empirical relations available in the literature to check for consistency within the error bars. Merloni & Heinz (2007) provided a relation between the jet kinetic power, estimated from the work done to inflate cavities in the surrounding X-ray emitting gas (see Allen et al. 2006; Rafferty et al. 2006; Cavagnolo et al. 2010), and the radio core luminosity at 5 GHz for their sample of low-luminosity radiatively inefficiently accreting sources hosting relativistic jets (e.g., FRI radio galaxies) as

$$\log P_{\text{jet,kin}} = (0.81 \pm 0.11) \log L_{\text{core},5\text{GHz}} + 11.9_{4.4}^{+4.1} \quad (3)$$

Using this equation and the radio core luminosity at 5 GHz, derived from the 10 GHz peak flux using the corresponding  $\alpha$ , the jet kinetic powers have been tabulated in Table 4. Both Foschini (2014) and Merloni & Heinz (2007) provide similar estimates of jet powers from the core luminosities within errors.

Additionally, we have estimated the jet bulk kinetic power using empirical relation given by Willott et al. (1999) (also see Rawlings & Saunders 1991; Falcke et al. 1995) where they found a tight correlation among the bulk kinetic power and narrow line region luminosity for radio-loud FRII sources. The relation is given as:

$$P_{\text{jet,kin}} \approx 3 \times 10^{38} L_{151}^{6/7} \text{ W}, \quad (4)$$

where  $L_{151}$  is the lobe radio luminosity at 151 MHz in the units of  $10^{28} \text{ W Hz}^{-1} \text{ Sr}^{-1}$ . We note that jet powers derived using 151 MHz luminosities from the TIFR GMRT Sky Survey (TGSS) and equation 4 above yielded similar numbers as from the other two methods.

Our selected sources being low luminosity and radiatively inefficiently accreting sources, though the presence of relativistic jets is not yet confirmed for all of them, Merloni & Heinz (2007) relations remain best-suited for determining the jet powers as used for other RQ sources or Seyferts (e.g., Doi et al. 2012; Zakamska & Greene 2014; Silpa et al. 2021b). The total jet power ( $P_{\text{jet}}$ ) is computed as the sum of  $P_{\text{jet,kin}}$  and  $P_{\text{jet,rad}}$  (see Angelakis et al. 2015). The estimated jet powers for our sample of Seyferts and LINERs are about 2 – 4 orders lower than the median of RL jets’ powers ( $> 10^{45} \text{ erg s}^{-1}$ ; Liu et al. 2006; Croston et al. 2018; Fan & Wu 2019). This suggests that apart from the very dense environment hindering the jet propagation for these sources, intrinsically these jets are low-powered consistent with inefficient accretion in these systems (Heckman & Best 2014; Berton et al. 2020).

#### 4.3. Energetics

Assuming equipartition between relativistic particles and magnetic fields, we could estimate the total radio luminosity ( $L_{\text{rad}}$ ), magnetic field strength ( $B_{\text{min}}$ ), total energy ( $E_{\text{Total}}$ ) of the particle and fields, and electron/particle lifetimes including synchrotron and IC CMB losses ( $\tau$ ), following the relations in O’Dea & Owen (1987); van der Laan & Perola (1969). In these calculations, the ratio of the ion energy to the electron energy ( $k$ ) and the volume filling factor ( $\phi$ ) are both assumed to be unity. The upper and lower cut-off frequencies ( $\nu_u$  and  $\nu_l$ ) are assumed to be 15 GHz and 100 MHz, respectively. The value of the function  $c_{12}$  in the equipartition calculation is obtained from Pacholczyk (1970). A cylindrical or spherical volume (for sources with circular morphology) is assumed for the sources. The equipartition estimates are presented in Table 3. These estimates are similar to those presented for other Seyfert galaxies and RQ AGN in the literature (e.g., Kharb et al. 2016; Silpa et al. 2021a; Rao et al. 2023). The errors in  $B_{\text{min}}$  and  $E_{\text{Total}}$  have been

estimated by propagating errors from  $\alpha$  and  $S_C$ . The B-field strengths in these sources range from 1 – 3  $\mu\text{G}$ , except for NGC 1068, which exhibits a high B-field of approximately 100  $\mu\text{G}$ , likely influenced by galactic B-field contributions. The total energy of these sources spans from  $10^{52}$  to  $10^{55}$  ergs, and the lifetimes of the relativistic particles range from  $10^5$  to  $10^7$  yr.

#### 4.4. Correlations

We present here the results of correlations between several global properties of our Seyfert and LINER sample. Due to the small sample size and to avoid biases due to outliers, we have primarily relied on Kendall’s Tau (KT) correlation test. We have also performed partial correlation tests to look for the dominance of a given parameter by accounting for the effects of others using the PYTHON package PINGOUIN for Spearman’s rank (SR) partial correlation test. To account for the upper limits, FORTRAN routines in the ASURV package (Lavalley et al. 1992) have been used. Survival analysis tests like the generalized KT test (Brown et al. 1973) was used for all the censored datasets. We note that discrepancies can arise in comparisons due to the varying methodologies used in deriving the literature values for these AGN. For instance,  $M_{\text{BH}}$  for most of type 1 AGN in this study has been estimated using the most reliable reverberation mapping technique. In contrast, type 2 AGN rely on more indirect methods, such as the black hole mass–stellar velocity dispersion relation or the BLR size–optical luminosity relation (see Woo & Urry 2002). This bias in the estimate may give rise to discrepancies in the correlations. In the cases of obvious outliers, we have assessed whether the correlations persist or change after removing outliers. For correlations involving polarization estimates, we have only considered the 10 sources with 10 GHz data for uniformity.

Our sample of Seyferts and LINERs are RQ sources and fall on the lower BH mass end compared to RL AGN (Laor 2000; Sikora et al. 2007). We find a strong correlation between  $R$  and the SMBH masses (KT test probability,  $p = 0.006$ ,  $r = 0.63$ ). The trend shown in Figure 15 follows a much tighter correlation than was obtained for a sample of Seyferts, LINERs, RL quasars and broad-line radio galaxies by Sikora et al. (2007), where  $R$  was as defined in Kellermann et al. (1989).

Figure 16 (left panel) shows that most sources in our sub-sample are core-dominated. However, a few sources exhibit luminous radio jets or lobes, viz., NGC 1068, NGC 4388, NGC 2992, NGC 3079, and NGC 3516 (listed in decreasing order of their lobe luminosities relative to their core luminosities). The total luminosity of NGC 1068 at 10 GHz is notably high, possibly due

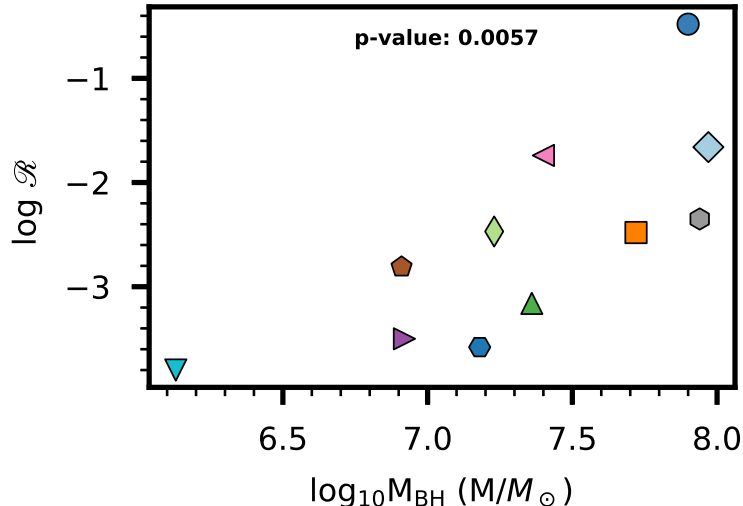


**Figure 15.** Radio loudness parameter versus black hole masses for 11 out of 12 sources in the selected sample. We did not have a proper estimate of radio loudness for NGC 4594 due to large uncertainties in the  $[\text{OIV}]\lambda 25.89 \mu\text{m}$  line luminosity and has thus been excluded. A strong correlation is found between  $R$  and  $M_{\text{BH}}$  for these sources (KT test with  $p = 0.0057$ ).

to the extrapolation from the 1.4 GHz value using the in-band  $\alpha$  value, the detection of more resolved components at 1.4 GHz with VLA BnA→A array observations, or contamination from galactic emission (though galactic contributions have been subtracted, some residuals may remain). The core luminosity at 10 GHz for the sample is found to be weakly correlated (KT test  $p = 0.03$ ) with the black hole masses as shown in the right panel of Figure 16.

Figure 17 (left panel) demonstrates a significant correlation between the polarized flux density and the core flux density at 10 GHz (KT test,  $p = 0.0041$ ). For comparing the polarised core and total flux densities, we have used average values within regions that are approximately the size of the synthesized beam at the centre. Higher polarized flux density typically arises from organized B-fields in the synchrotron plasma. Intrinsically randomized B-fields can reduce overall polarized intensity. Additionally, external Faraday rotating media can decrease polarized flux density by randomizing the polarization angles. The observed correlation between total intensity and polarized intensity at the core suggests that sources with more organized B-fields tend to be more luminous in radio.

Although polarized emission is typically not detected in the core regions, it is detected with a high SNR in the extended regions ( $\sim\text{kpc}$  scales) for all sources. To calculate the polarized flux densities in the extended region, we subtracted the core’s contribution from the total polarized emission. The KT test shows a moderate correlation with  $p = 0.019$  with the core flux density (see Table 6). The  $f_p$  indicator (see Figure 17, right panel) shows that the extended structures are highly polarized,

suggesting a dependence of the kpc-scale B-field ordering in the jets or lobes of these AGN.

The Eddington luminosity for the sources has been obtained using the relation (Rybicki & Lightman 1979):

$$L_{\text{Edd}}(\text{in erg/s}) = 1.26 \times 10^{38} M_{\text{BH}}/M_{\odot} \quad (5)$$

We further obtained the Eddington ratio as  $\lambda_{\text{Edd}} = L_{\text{bol}}/L_{\text{Edd}}$ , where  $L_{\text{bol}}$  is obtained as in Table 1. Since we do not have direct estimates of the accretion rates for these sources, we assume  $\lambda_{\text{Edd}}$  to represent the accretion scenario. We compared the values obtained from our radio-polarimetric observations with the intrinsic properties of the central engine to identify the primary factors responsible for producing KSRs from RQ nuclei.

Figure 18 shows the distribution of core spectral indices versus the Eddington ratios for the sources. The in-band  $\alpha$  image of NGC 4593 (Figure 12; right panel) is complex; apart from the likely presence of an inverted spectrum core slightly offset from the peak radio emission, a spectral steepening is observed in east-west direction north of the peak emission region, consistent with the small double-jetted source observed in the higher resolution image of Gallimore et al. (2004). We observe a bimodality in the spectral index distribution with respect to Eddington ratios after excluding the source NGC 4593. Although we note that after combining the 3 GHz data from Rao et al. (2023) and our work, the integrated  $\alpha$  value obtained for NGC 4593 is  $-0.48 \pm 0.04$ , which would also make NGC 4593 fall in the bottom right quadrant along with the majority of the sources. We have defined  $\alpha > -0.3$  to be flat and  $\alpha < -0.3$  to be a steep spectral index. We find that sources with higher  $\lambda_{\text{Edd}} (> 2.5 \times 10^{-3})$  have a steep spectrum core, whereas

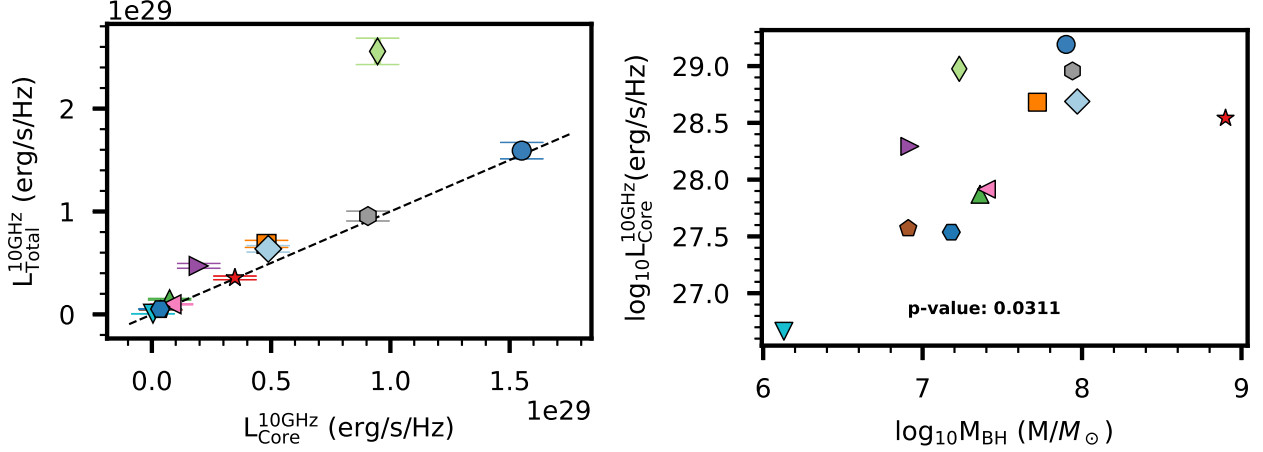


**Figure 16.** (Left) Total luminosity versus core luminosity at 10 GHz. The black dashed line indicates the slope equal to unity. (Right) Core luminosity at 10 GHz versus black hole mass. A marginal correlation is observed with KT test  $p = 0.0311$ . Error bars are noted along with the symbols.

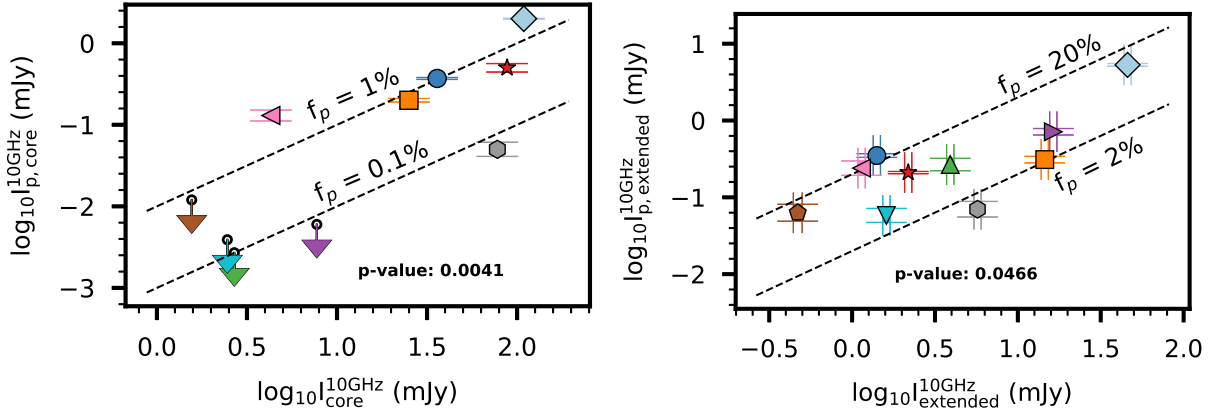


**Figure 17.** (Left) Logarithm of polarized flux density versus logarithm of total flux density in the core at 10 GHz. The errors on  $\log_{10}y$ -value have been calculated as  $(\text{errors on } y\text{-value}) / (y\text{-value} \times \log_e 10)$  using error propagation methods. The generalized KT test indicates a significant correlation with  $p = 0.0041$ . The dashed lines show the various fractional polarization values. (Right) Logarithm of polarized flux density from extended emission (excluding the core) versus the logarithm of total flux density at 10 GHz. The KT test shows a mild correlation with  $p = 0.0466$ . Error bars are noted along with the symbols, and upper limits are noted as downward-facing arrows.

lower Eddington ratio sources appear to have a flat core. A similar trend has been observed for other RQ sources (e.g., Laor et al. 2019) suggesting a common physical driver linking these two quantities. Notably, most of the compact sources in our sample exhibit steep spectra. This could be due to presence of jets in these sources which are not resolved in our images (e.g., O’Dea 1998; Moran 2000; O’Dea & Saikia 2021).

We observe a marginal correlation between the total energy (particle + B-fields) and the black hole masses (see Figure 19, left panel). The best-fit line has a slope of 0.62 and an intercept of 49.27 with a standard deviation of 0.5. No correlation was found between other equipartition estimates and the intrinsic properties of the central engine. Since total energy is related to (radiative)

jet power, this correlation suggests a dependence of jet power on black hole mass as has also been found by McLure et al. (2004); Chen et al. (2015) in RL sources. Additionally, we found a strong correlation ( $p = 0.0008$  with partial SR test, see Table 6) between the jet kinetic power, derived using the method of Merloni & Heinz (2007), and black hole mass (see also Liu et al. 2006). This indicates that black hole mass is a major driver for jets in RQ AGN with KSRs.

The ratio of jet kinetic power to Eddington luminosity shows a weak correlation with the Eddington ratio (see Figure 19, right panel). This relationship can be expressed as  $P_{\text{jet,kin}}/L_{\text{Edd}} = (0.29 \pm 0.09)\lambda_{\text{Edd}} - (2.29 \pm 0.21)$ . This observed dependence has a shallower slope than that reported by Merloni & Heinz (2007), who sug-

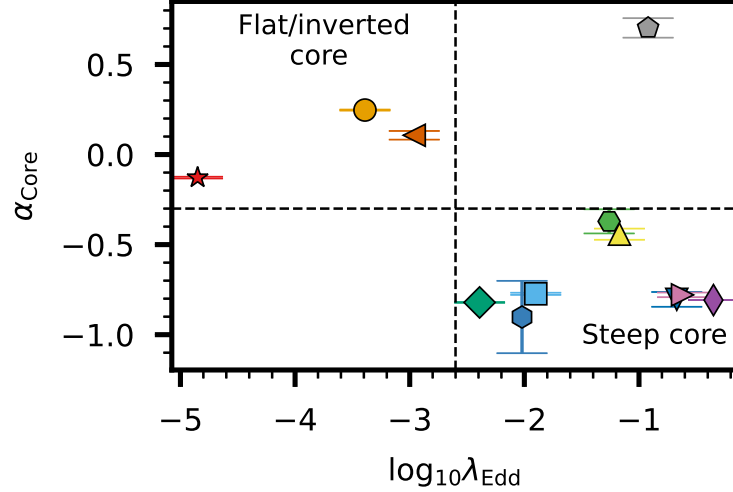


**Figure 18.** In-band core spectral indices versus the Eddington ratios. The horizontal black dashed line indicates a spectral index of  $-0.3$ . The vertical dashed line indicates the central value ( $[\text{minimum} + \text{maximum}]/2$ ) of  $\lambda_{Edd}$ . Values greater than  $\alpha = -0.3$  are considered flat while lower values are considered steep. Error bars are noted along with the symbols.

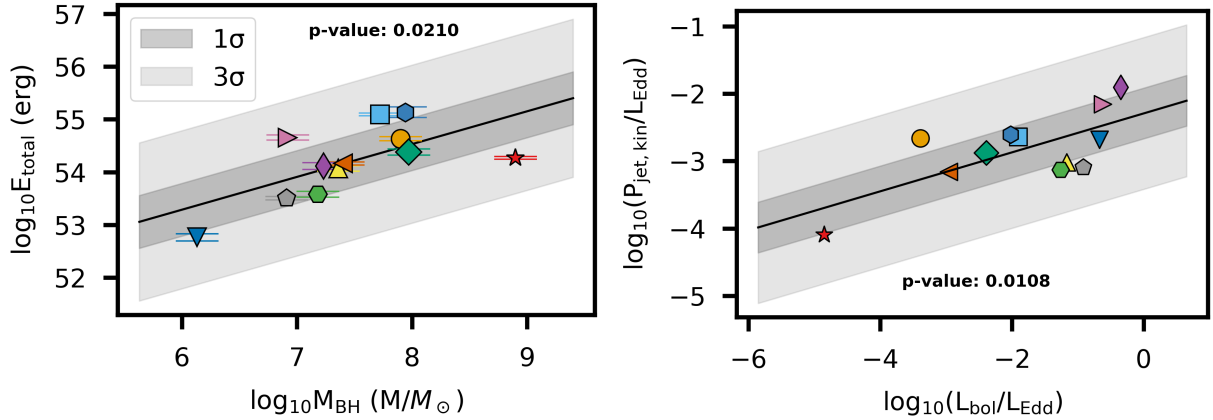


**Figure 19.** (Left) Total energy (particle + fields) versus the black hole mass in log-log scale. The KT test indicates a marginal correlation ( $p = 0.0210$ ). A linear regression model has been fit here to obtain the best-fit line shown in black. The  $1\sigma$ ,  $3\sigma$  and  $5\sigma$  standard deviations are shown with filled regions of different transparencies. (Right) The ratio of kinetic jet power to Eddington luminosity versus the ratio of bolometric luminosity to Eddington luminosity in log-log scale. The KT test suggests a weak correlation ( $p = 0.0628$ ). A linear regression model with the best-fit line shown in black suggests a slightly stronger correlation ( $p = 0.0108$ ). The  $1\sigma$  and  $3\sigma$  standard deviations are shown with filled regions of different transparencies. Error bars are noted along with the symbols.

gested a radiatively inefficient accretion flow as proposed by Fender et al. (2003). This dissimilarity may indicate that the Seyfert and LINER galaxies in our sample are not as dominated by relativistic jets as the low luminosity RL sources investigated by Merloni & Heinz (2007). Rather, only a fraction of the bolometric luminosity is converted into jet kinetic and radiative power in the RQ sources consistent with Padovani (2017).

We observe a strong correlation between the core polarized flux density and Eddington ratios (Figure 20; top left panel; generalized KT test  $p = 0.007$ ). The best-fit line has a slope of  $-0.82$ , intercept of  $-3.29$  and a stan-

dard deviation of 0.85. Notably, the core polarization intensity for NGC 3079 is significantly high, exceeding the  $1\sigma$  deviation, which is consistent with its high total intensity at the core. To account for the bias from the total radio emission, we have also plotted the core polarization fraction against Eddington ratios (Figure 20; top right panel). This analysis reveals a moderate correlation (generalized KT test  $p = 0.029$ ; partial SR test  $p = 0.025$ , keeping  $M_{BH}$  fixed). The best-fit line has a slope of  $-0.62$ , intercept  $= -0.89$  and standard deviation  $= 1.1$ . These correlations suggest that B-field ordering in the core regions is higher in the lower accretion sys-

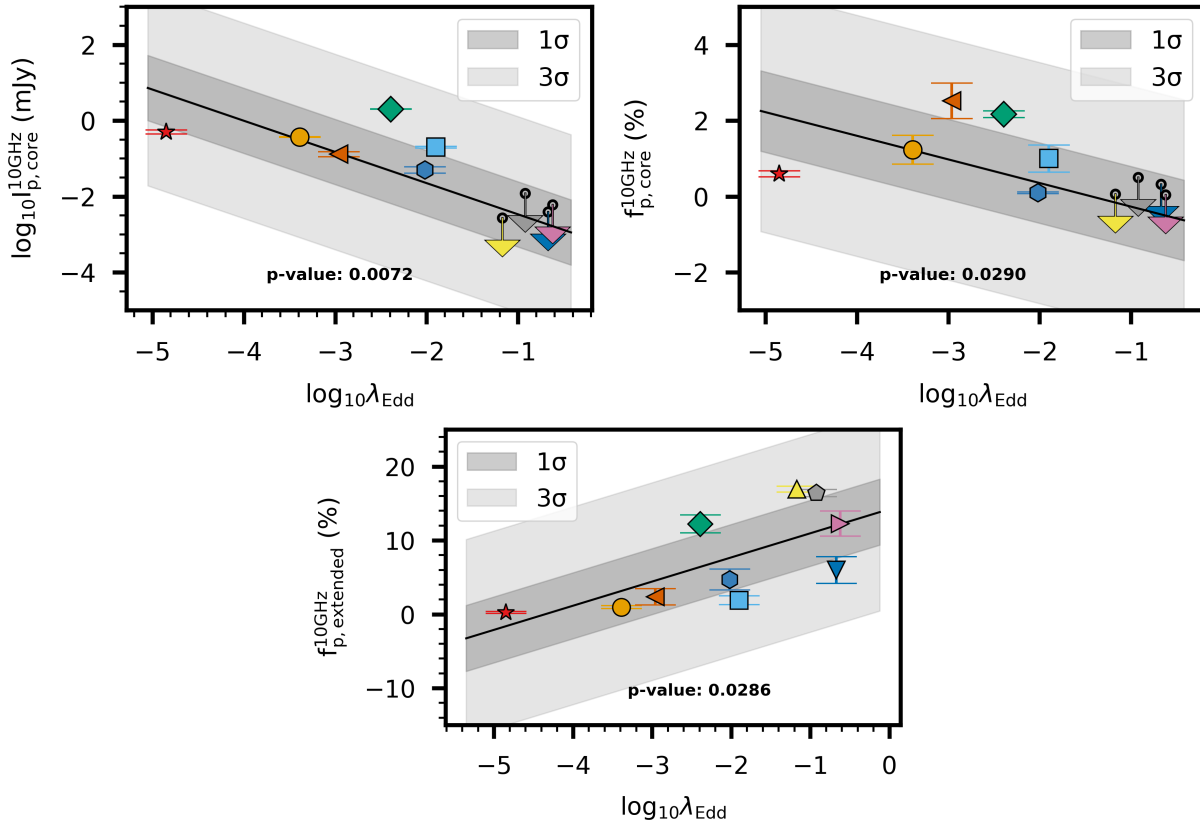


**Figure 20.** (Top left) Log-log plot of the core polarized flux density versus the Eddington ratios. The generalized KT test indicates a strong correlation ( $p = 0.0072$ ). A linear regression model has been fit here to obtain the best-fit line shown in black. The  $1\sigma$  and  $3\sigma$  deviations are shown with filled regions of different transparencies. (Top right) Plot of core fractional polarization versus logarithm of the Eddington ratios. The generalized KT test indicates a correlation ( $p=0.0290$ ). The linear regression model best-fit line is shown in black with parameters: slope =  $-0.57$ , intercept =  $0.08$ , standard error =  $0.19$ . The  $3\sigma$  and  $5\sigma$  standard deviations are shown with filled regions of different transparencies. (Bottom) Polarization fraction for the extended emission (excluding the core) versus logarithm of the Eddington ratios. The KT test indicates a weak positive correlation with  $p=0.0286$ . Error bars are noted along with the symbols, and the upper limits are noted as downward facing arrows.

tems. This can be possible because higher accretion may accumulate more Faraday rotating and hence depolarising material in the core regions. Overall, these results may indicate that in lower accretion systems, wind-like outflows are also present along with the jets. This results in decreasing the B-field ordering as well as polarized intensity (e.g., [Silpa et al. 2021b, 2022](#)). On the other hand, Figure 20 (bottom panel) shows a positive correlation between polarization fraction and Eddington ratios in the extended radio lobes (KT test  $p=0.029$ ). This may suggest that higher accreting sources produce radio emission with more ordered B-field structures.

The current work presents a small sample size, hence the above correlation results represent small-number statistics, potentially applicable to the RQ population of low-luminosity AGN showing larger extents of radio emission. In the future, we intend to include the remaining sources from the sample, adding more KSRs

and point sources at  $\sim 15''$  resolution, to provide a more comprehensive analysis of the entire population of Seyferts and LINERs with significant AGN contributions.

## 5. DISCUSSION

The origin of radio emission in RQ AGN remains a topic of significant investigation and debate after years of study ([Ishibashi & Courvoisier 2011](#); [Zakamska & Greene 2014](#); [Panessa et al. 2019](#); [Radcliffe et al. 2021](#)). Unlike RL AGN exhibiting powerful radio jets extending far beyond the host galaxy into the IGM, RQ AGN typically show much more compact radio emissions, which makes them more difficult to study and understand. Understanding the origin of the radio emission in these RQ sources is crucial not only for interpreting these systems but also for comprehending AGN feedback and galaxy evolution, as these constitute the dominant ( $\sim 80\%$ ) population of the AGN. AGN feedback, which includes both

the release of energy into the surrounding medium and the regulation of star formation and black hole growth (King & Pounds 2015), is less obvious and harder to detect in RQ AGN (Santoro et al. 2020; Harrison & Ramos Almeida 2024). The following sub-sections discuss the properties of the selected sample and their relation with the host galaxies.

### 5.1. Radio-FIR correlation

Most of the sources in the studied sample lie above the tight radio-FIR correlation derived by Yun et al. (2001) for a large sample of AGN and star-forming galaxies, indicating that starburst activity alone cannot account for the observed radio excess in these galaxies (Gallimore et al. 2006a; Sebastian et al. 2020). Typically, radio emission from stellar activity and winds exhibits a morphology similar to that of the host galaxy (Panessa et al. 2019). While this is observed in some of the sample sources, the Seyfert outflow is often oriented at a large angle to the galactic radio continuum.

### 5.2. Star formation rates

We have estimated the star formation rates in these galaxies using the relation  $SFR = 4.5 \times 10^{-44} L_{FIR}$  (Kennicutt 1998),  $L_{FIR} = (1 + S_{100\mu m} / 2.58 S_{60\mu m}) L_{60\mu m}$  (Helou et al. 1988; Yun et al. 2001), and FIR luminosities from Fullmer & Lonsdale (1989); Moshir & et al. (1990); Moshir et al. (1993). The SFR in these Seyfert and LINER galaxies are approximately  $1 - 2 M_{\odot}/yr$  except in NGC 1068 ( $\sim 14 M_{\odot}/yr$ ), NGC 3079 ( $\sim 4 M_{\odot}/yr$ ) and NGC 4388 ( $\sim 4 M_{\odot}/yr$ ), where radio emission from the galactic disk is also detected. Therefore, the observed radio synchrotron emission in these galaxies with KSRs can be attributed to AGN-driven jets and winds, rather than starburst superwinds.

### 5.3. Polarization and B-field properties

We have detected polarized emission in all the sources. The sources with detected galactic emission clearly show a difference in the fractional polarization compared to the Seyfert or LINER radio outflow. The highly polarized extended radio emission, displaying a well-ordered B-field structure anchored to the central engine, supports the suggestion that these KSRs are AGN-driven (e.g., Sebastian et al. 2020).

Jets can be launched by extracting energy from the rotating SMBH, where B-fields are twisted and amplified by the black hole, generating a strong Poynting flux (Blandford & Znajek 1977; Qian et al. 2018, BZ mechanism). Alternatively, jets can derive energy from the accretion disk, generating strong toroidal B-fields that drive the jet through magnetocentrifugal forces (Bland-

ford & Payne 1982, BP mechanism), or through a combination of both mechanisms (Wang et al. 2008; Garofalo et al. 2010; Talbot et al. 2021). The BZ mechanism is thought to be more effective for high black hole spin parameters and is often associated with launching axial jets (Wang et al. 2008; Qian et al. 2018), whereas the BP mechanism is more effective for lower black hole spin parameters and is often associated with launching disk winds (Li et al. 2008; Qian et al. 2018). AGN-driven winds refer to magnetically-driven outflows that can be the broadened base of the jet (Mehdipour & Costantini 2019; Silpa et al. 2021b), the broken/decollimated part of the jet (Veilleux et al. 2005; Mukherjee et al. 2018), or from the inner accretion disk (Fukumura et al. 2010), rather than radiatively/thermally-driven winds from the accretion disk/torus/BLR (e.g., Begelman et al. 1983; Proga & Kallman 2004; Mizumoto et al. 2019). Our study supports the suggestion of jet launching accompanied either by an accretion disk wind or broadened jets with transverse velocity structures. Based on the jet simulation studies of Tchekhovskoy & Bromberg (2016); Barniol Duran et al. (2017), the magnetic field structures observed in our sources may support the presence of the BZ mechanism.

The 10 GHz  $\sim 7''$  cores of most of the Seyfert galaxies (e.g., NGC 3516, NGC 4593, NGC 5506, NGC 1320) are unpolarized in our observations to within  $\sim 10 \mu Jy \text{ beam}^{-1}$ . This may be due to the presence of denser material (cold gas) in the cores causing Faraday depolarization (Contopoulos et al. 2015), inhomogeneous polarised emission, or Faraday rotation within the source depth (Cioffi & Jones 1980). Those with detected polarization (e.g., NGC 4235, NGC 4388, NGC 4594) primarily show an inferred toroidal field component in the cores. This may suggest the presence of AGN winds or jet sheaths along with the jets in these sources (e.g., Mehdipour & Costantini 2019; Silpa et al. 2021b). The presence of winds or sheaths may in turn be the cause of the stunted growth of the jets, as they act like a cocoon around the jet and hinder the jet's motion.

In several sources (e.g., NGC 1320, NGC 3516, NGC 3079, NGC 4388), we observe jet bending with the B-field lines following the bend suggesting that poloidal magnetic fields are 'frozen' in the synchrotron plasma of the jet. Moreover, jet bending may suggest that the denser environment in the spiral host galaxies of Seyferts or LINERs can be an important factor in their stunted growth (Gallimore et al. 2006b; Nolting et al. 2019; Silpa et al. 2023). In some sources, the dense medium causes the jet to break up and channel through the medium into the IGM along the least hindered paths (e.g., Saxton et al. 2005; Mukherjee et al. 2018).

**Table 6.** Correlations and probability (p) values

Quantity 1	Quantity 2	p-value	Correlation coefficient	Test type
$M_{\text{BH}}$	$\lambda_{\text{Edd}}$	0.0001	-0.91	Partial SR keeping all fixed
$P_{\text{jet,kin}}$	$M_{\text{BH}}$	0.0008	0.85	Partial SR keeping $\lambda_{\text{Edd}}$ fixed
$P_{\text{jet,kin}}$	$\lambda_{\text{Edd}}$	0.0123	0.72	Partial SR keeping $M_{\text{BH}}$ fixed
$f_{\text{p,core}}$	$M_{\text{BH}}$	0.2145	0.43	Partial SR keeping $\lambda_{\text{Edd}}$ fixed
$f_{\text{p,core}}$	$\lambda_{\text{Edd}}$	0.0251	-0.70	Partial SR keeping $M_{\text{BH}}$ fixed
$f_{\text{p,extended}}$	$M_{\text{BH}}$	0.067	-0.6	Partial SR keeping $\lambda_{\text{Edd}}$ fixed
$f_{\text{p,extended}}$	$\lambda_{\text{Edd}}$	0.0133	0.75	Partial SR keeping $M_{\text{BH}}$ fixed
$P_{\text{jet,kin}}$	$M_{\text{BH}}$	0.0209	0.52	KT
$P_{\text{jet,kin}}$	$\lambda_{\text{Edd}}$	0.3807	-0.21	KT
$P_{\text{jet,kin}}/L_{\text{Edd}}$	$\lambda_{\text{Edd}}$	0.0108	0.70	Linear regression*
$R$	$M_{\text{BH}}$	0.0057	0.63	KT
$L_{\text{core,10GHz}}$	$M_{\text{BH}}$	0.0311	0.48	KT
$L_{\text{bol}}$	$M_{\text{BH}}$	0.0287	-0.51	KT
$B_{\text{min}}$	$M_{\text{BH}}$	0.6384	0.12	KT
$E_{\text{total}}$	$M_{\text{BH}}$	0.0210	0.51	KT
$\tau$	$M_{\text{BH}}$	0.7373	-0.09	KT
$I_{\text{p,core}}$	$I_{\text{core}}$	0.0041	2.874 <sup>†</sup>	Generalized KT
$I_{\text{p,extended}}$	$I_{\text{extended}}$	0.0466	0.51	KT
$I_{\text{p,extended}}$	$I_{\text{core}}$	0.0196	0.58	KT
$I_{\text{p,core}}$	$\lambda_{\text{Edd}}$	0.0072	2.69 <sup>†</sup>	Generalized KT
$f_{\text{p,core}}$	$\lambda_{\text{Edd}}$	0.0290	2.183 <sup>†</sup>	Generalized KT
$f_{\text{p,extended}}$	$\lambda_{\text{Edd}}$	0.0286	0.553	KT

*Note:* SR = Spearman’s rank test, KT = Kendall’s Tau, \*linear regression by EM algorithm from ASURV package, <sup>†</sup>z-value from Generalized KT test (O’Brien 1978).  $M_{\text{BH}}$  is the mass of the black hole,  $\lambda_{\text{Edd}}$  is the Eddington ratio,  $P_{\text{jet,kin}}$  is the jet kinetic power,  $f_{\text{p,core}}$  is the core fractional polarization,  $L_{\text{Edd}}$  is the Eddington luminosity,  $R$  is the radio luminosity,  $L_{\text{core,10GHz}}$  is the core luminosity at 10 GHz,  $L_{\text{bol}}$  is the bolometric luminosity,  $B_{\text{min}}$  is the magnetic field under equipartition condition,  $E_{\text{total}}$  is the total energy under equipartition condition,  $\tau$  is the electron lifetime with synchrotron and IC CMB losses,  $I_{\text{p,core}}$  is polarized intensity at the core,  $I_{\text{p,extended}}$  is the polarized intensity in the extended region including the jets and the lobes, and  $f_{\text{p,extended}}$  is the fractional polarization in the same region.

The inferred B-field orientations in the radio outflows of all the Seyfert and LINER galaxies presented here support the presence of ordered B-fields even on kpc-scales. The B-field structures observed in some sources (e.g., NGC 3516) are similar to those observed in RL FR II radio galaxies where the hotspot shows B-field compression perpendicular to the jet direction (e.g., Conway et al. 1993; Kharb et al. 2008; Baghel et al. 2023). The hotspot in NGC 3516 additionally shows a spectral index flattening signifying particle re-acceleration at the terminal shock region of the radio outflow. This suggests that some RQ sources are not intrinsically different from RL sources in terms of their jet-launching mechanisms.

#### 5.4. Host-AGN association

The Seyfert-starburst composite galaxy NGC 3079 shows a lack of atomic neutral hydrogen gas along the Seyfert outflow direction indicating that AGN activity is either ionizing or pushing away gas, depleting the neutral hydrogen gas reservoir. This in turn quenches star formation along the radio outflow. On the other hand, in NGC 4388, we observe an extension of the H $\alpha$  gas along the jet, which may indicate the presence of star-forming regions along the jet. Additionally, the second fainter component of H $\alpha$  in NGC 2992 coincides with the region of possible ‘relic’ emission. Similarly, we see [O III] 5007Å emission (Schmitt et al. 2003) following

the S-shape of the Seyfert radio jet in NGC 3516 but on smaller scales, which may indicate cold gas entrainment by the jet. Therefore, overall, we observe a close connection between the emission-line gas and radio outflows, and an indication of both positive and negative AGN feedback, similar to those seen in numerical simulations of jets by Mukherjee et al. (2018); Meenakshi et al. (2023).

### 5.5. Drivers of the radio outflow

The radio outflow properties in our small sample show a strong connection with the black hole masses. Both the jet power and the total energy (particle + B-field energy) correlate strongly with  $M_{BH}$ , but not significantly with  $\lambda_{Edd}$  when checked using partial SR test. This indicates that the driving factor is the mass of the black holes rather than the accretion rate. The correlation suggests that the B-field strength at the jet launching sites is stronger for sources with higher black hole masses, resulting in stronger jets. This finding potentially supports the BZ mechanism of jet launching (see Tchekhovskoy & Bromberg 2016).

We observe a bimodality in terms of Eddington ratios. Radio cores with flatter spectra are associated with sources with lower Eddington ratios, whereas the steeper cores are associated with higher Eddington ratios (also observed in Laor & Behar 2008; Chen et al. 2023). Similarly, an anti-correlation is observed between the polarization fraction and the Eddington ratios (partial correlation test  $p = 0.025$ , see Table 6) in the cores. This could be consistent with greater Faraday-rotating medium and greater net depolarization closer to the jet launching sites in highly accreting sources, or more radiation-pressure-driven winds in them. Interestingly, we observe a weak positive trend in the fractional polarization versus Eddington ratios (partial SR correlation test  $p = 0.013$ ) for lobe emission. This may suggest that higher accreting sources are more effective at sustaining ordered magnetic fields on larger spatial scales.

Low-luminosity AGN are hypothesized to possess inner radiatively inefficient accreting flow (RIAF) disk and outer thin disk systems (Lasota et al. 1996; Ho et al. 2000; Ho 2008). Moreover, the study by Ho (2009) suggests that RIAF systems power Seyferts/LINERs with radiative efficiency much less than 0.1. This implies that higher Eddington ratio sources, although accreting at a higher rate, cannot efficiently convert gravitational potential energy to radiative energy. Rather a significant part of the accretion power gets advected onto the black hole (advection-dominated accretion flow, ADAF; Narayan et al. 1998) or gets transferred to jet power (e.g., Falcke et al. 2001). The spectral steepening with

higher  $\lambda_{Edd}$  supports the idea that sources with flatter core spectra are currently in an active jet phase, accreting via ADAF/RIAF modes. In contrast, sources with steeper cores likely experienced jet activity in the past and are now accreting efficiently in a radiatively dominant mode.

## 6. SUMMARY & CONCLUSIONS

In this paper, we have presented radio polarimetric images of 12 Seyfert galaxies with KSRs belonging to the CfA+12 micron sample at 1.4–6 GHz and 10 GHz using the VLA BnA→A or D array configurations, respectively. We have attempted to understand the origin and impact of the radio outflows from these RQ AGN. The outcomes of this study are summarised below.

1. Bubble-like or lobe-like radio structures with dominant cores are detected in the 12 sources. The in-band spectral indices range from inverted to steep ( $\alpha \sim +0.5$  to  $-1.2$ ) at the core. We find signatures of organized B-field structures in the kpc-scale cores, jets, and lobes of these galaxies with the fractional polarization varying between a few per cent in the radio cores to up to  $47 \pm 18\%$  in the lobes. These results are consistent with the AGN being the primary driver of radio outflows in these galaxies.
2. In the four galaxies showing host galaxy emission along with the KSRs, viz., NGC 4388, NGC 3079, NGC 4594, and NGC1068, the apparent B-fields are aligned along the spiral arms of the galactic disks with the degrees of polarization typically being lower than the KSR values in that source.
3. Based on global correlations we find a strong correlation between the mass of the supermassive black holes and the radio outflow properties like jet kinetic power, with accretion rate playing a secondary role in these RQ sources. This further attests to the dominance of AGN jets in producing KSRs in Seyfert and LINER galaxies.
4. We find a significant correlation between total and polarized core intensities in these sources. This implies that a more organized B-field which results in greater polarized emission also produces a more luminous radio source. This attests to the existence of dominant MHD outflows in RQ AGN. The B-fields are inferred to be toroidal in the cores of several sources which could suggest the presence of either a jet sheath surrounding the jet spine or a wind component surrounding the jet. The spectral

index versus Eddington ratio relation is consistent with this suggestion.

5. An anti-correlation is observed between the core fractional polarization and Eddington ratios. This could suggest the presence of greater depolarizing media in sources with greater accretion rates, or more radiation-pressure-driven winds in them. A weak positive trend in the fractional polarization versus Eddington ratios for lobe emission, on the other hand, may suggest that higher accreting sources are more effective at sustaining ordered magnetic fields on kpc-scales.
6. An examination of the radio properties along with emission line gas reveals the signatures of both positive and negative jet-related AGN feedback in these sources (e.g., NGC 3079, NGC 2992). This supports the idea that radio-quiet AGN can significantly impact their host galaxy environments in spite of producing smaller outflows.
7. Several sources show the signatures of jet bending, flaring or disruption indicating strong jet-medium interaction. The spectra and/or polarization structures indicate the presence of relic lobes and thereby episodic AGN activity in some of the sources (e.g., NGC 1068, NGC 2992, NGC 4593).

Overall, we find that AGN-related radio outflows are prominent in radio-quiet AGN and could be driven by

strong magnetic fields anchored to the black holes themselves. These jets interact strongly with their surrounding media which in turn affects their total radio extents making them radio-quiet.

## 7. ACKNOWLEDGEMENTS

We thank the referee for their suggestions which have improved this manuscript significantly. SG and PK acknowledge the support of the Department of Atomic Energy, Government of India, under the project 12-R&D-TFR-5.02-0700. SB and CO acknowledge support from the Natural Sciences and Engineering Research Council (NSERC) of Canada. This research has used data from the National Radio Astronomy Observatory (NRAO) facility. NRAO is the facility of the National Science Foundation operated under a cooperative agreement by Associated Universities, Inc. We thank the staff of the GMRT that made these observations possible. GMRT is run by the National Centre for Radio Astrophysics of the Tata Institute of Fundamental Research. This research has made use of the NASA/IPAC Extragalactic Database (NED), which is operated by the Jet Propulsion Laboratory, California Institute of Technology, under contract with the National Aeronautics and Space Administration.

## REFERENCES

- Abdo, A. A., Ackermann, M., Ajello, M., et al. 2009, *ApJL*, 707, L142
- Abell, G. O., Eastmond, T. S., & Jenner, D. C. 1978, *ApJL*, 221, L1
- Allen, S. W., Dunn, R. J. H., Fabian, A. C., Taylor, G. B., & Reynolds, C. S. 2006, *MNRAS*, 372, 21
- Angelakis, E., Fuhrmann, L., Marchili, N., et al. 2015, *A&A*, 575, A55
- Antonucci, R. 1993, *ARA&A*, 31, 473
- Antonucci, R. R. J., & Miller, J. S. 1985, *ApJ*, 297, 621
- Baghel, J., Kharb, P., Silpa, Ho, L. C., & Harrison, C. M. 2023, *MNRAS*, 519, 2773
- Bajaja, E., Dettmar, R. J., Hummel, E., & Wielebinski, R. 1988, *A&A*, 202, 35
- Baldwin, J. A., Phillips, M. M., & Terlevich, R. 1981, *PASP*, 93, 5
- Balzano, V. A. 1983, *ApJ*, 268, 602
- Bandyopadhyay, B., Xie, F.-G., Nagar, N. M., et al. 2019, *MNRAS*, 490, 4606
- Barniol Duran, R., Tchekhovskoy, A., & Giannios, D. 2017, *MNRAS*, 469, 4957
- Baum, S. A., O’Dea, C. P., Dallacassa, D., de Bruyn, A. G., & Pedlar, A. 1993, *ApJ*, 419, 553
- Begelman, M. C., McKee, C. F., & Shields, G. A. 1983, *ApJ*, 271, 70
- Berton, M., Järvelä, E., Crepaldi, L., et al. 2020, *A&A*, 636, A64
- Blandford, R. D., & Königl, A. 1979, *ApJ*, 232, 34
- Blandford, R. D., & Payne, D. G. 1982, *MNRAS*, 199, 883
- Blandford, R. D., & Rees, M. J. 1978, *PhyS*, 17, 265
- Blandford, R. D., & Znajek, R. L. 1977, *MNRAS*, 179, 433
- Bridle, A. H., Hough, D. H., Lonsdale, C. J., Burns, J. O., & Laing, R. A. 1994, *AJ*, 108, 766

- Brown, B., Hollander, M., Korwar, R., & of STATISTICS., F. S. U. T. D. 1973, Nonparametric Tests of Independence for Censored Data with Application to Heart Transplant Studies (Defense Technical Information Center).  
<https://books.google.co.in/books?id=o-h-NwAACAAJ>
- Cavagnolo, K. W., McNamara, B. R., Nulsen, P. E. J., et al. 2010, *ApJ*, 720, 1066
- Cawthorne, T. V., & Hughes, P. A. 2013, *ApJ*, 771, 60
- Cecil, G., Bland-Hawthorn, J., & Veilleux, S. 2002, *ApJ*, 576, 745
- Cecil, G., Bland-Hawthorn, J., Veilleux, S., & Filippenko, A. V. 2001, *ApJ*, 555, 338
- Chen, S., Laor, A., Behar, E., Baldi, R. D., & Gelfand, J. D. 2023, *MNRAS*, 525, 164
- Chen, S., Kharb, P., Silpa, S., et al. 2024, *ApJ*, 963, 32
- Chen, Y.-Y., Zhang, X., Xiong, D., & Yu, X. 2015, *AJ*, 150, 8
- Christopoulou, P. E., Holloway, A. J., Steffen, W., et al. 1997, *MNRAS*, 284, 385
- Chung, A., van Gorkom, J. H., Kenney, J. D. P., Crowl, H., & Vollmer, B. 2009, *AJ*, 138, 1741
- Cioffi, D. F., & Jones, T. W. 1980, *AJ*, 85, 368
- Clavel, J., Joly, M., Collin-Souffrin, S., Bergeron, J., & Penston, M. V. 1983, *MNRAS*, 202, 85
- Colbert, E. J. M., Baum, S. A., Gallimore, J. F., O’Dea, C. P., & Christensen, J. A. 1996a, *ApJ*, 467, 551
- Colbert, E. J. M., Baum, S. A., Gallimore, J. F., et al. 1996b, *ApJS*, 105, 75
- Condon, J. J., Cotton, W. D., Greisen, E. W., et al. 1998, *AJ*, 115, 1693
- Contopoulos, I., Gabuzda, D., & Kylafis, N., eds. 2015, *Astrophysics and Space Science Library*, Vol. 414, *The Formation and Disruption of Black Hole Jets*, ed. I. Contopoulos, D. Gabuzda, & N. Kylafis (Springer)
- Conway, R. G., Garrington, S. T., Perley, R. A., & Biretta, J. A. 1993, *A&A*, 267, 347
- Corbin, M. R., Baldwin, J. A., & Wilson, A. S. 1988, *ApJ*, 334, 584
- Croston, J. H., Ineson, J., & Hardcastle, M. J. 2018, *MNRAS*, 476, 1614
- de Bruyn, A. G., & Wilson, A. S. 1976, *A&A*, 53, 93
- De Robertis, M. M., & Osterbrock, D. E. 1986, *ApJ*, 301, 98
- Dietrich, M., Kollatschny, W., Alloin, D., et al. 1994, *A&A*, 284, 33
- Doi, A., Nagira, H., Kawakatu, N., et al. 2012, *ApJ*, 760, 41
- Dong, X. Y., & De Robertis, M. M. 2006, *AJ*, 131, 1236
- Duc, P. A., Brinks, E., Springel, V., et al. 2000, *AJ*, 120, 1238
- Dumas, G., Mundell, C. G., Emsellem, E., & Nagar, N. M. 2007, *MNRAS*, 379, 1249
- Durret, F., & Bergeron, J. 1987, *A&A*, 173, 219
- Esposito, F., Alonso-Herrero, A., García-Burillo, S., et al. 2024, *A&A*, 686, A46
- Falcke, H., Malkan, M. A., & Biermann, P. L. 1995, *A&A*, 298, 375
- Falcke, H., Nagar, N. M., Wilson, A. S., Ho, L. C., & Ulvestad, J. S. 2001, in *Black Holes in Binaries and Galactic Nuclei*, ed. L. Kaper, E. P. J. V. D. Heuvel, & P. A. Woudt, 218
- Fan, X.-L., & Wu, Q. 2019, *ApJ*, 879, 107
- Fender, R. P., Gallo, E., & Jonker, P. G. 2003, *MNRAS*, 343, L99
- Ferruit, P., Wilson, A. S., & Mulchaey, J. 2000, *ApJS*, 128, 139
- Filippenko, A. V. 1992, in *Astronomical Society of the Pacific Conference Series*, Vol. 31, *Relationships Between Active Galactic Nuclei and Starburst Galaxies*, ed. A. V. Filippenko, 253
- Fischer, T. C., Crenshaw, D. M., Kraemer, S. B., & Schmitt, H. R. 2013, *ApJS*, 209, 1
- Fischer, T. C., Johnson, M. C., Secretst, N. J., Crenshaw, D. M., & Kraemer, S. B. 2023, *ApJ*, 953, 87
- Foschini, L. 2012, in *International Journal of Modern Physics Conference Series*, Vol. 8, *International Journal of Modern Physics Conference Series*, 172–177
- Foschini, L. 2014, in *International Journal of Modern Physics Conference Series*, Vol. 28, *International Journal of Modern Physics Conference Series*, 1460188
- Fukumura, K., Kazanas, D., Contopoulos, I., & Behar, E. 2010, *ApJ*, 715, 636
- Fullmer, L., & Lonsdale, C. J. 1989, *JPL D-1932*, 0
- Gallimore, J. F., Axon, D. J., O’Dea, C. P., Baum, S. A., & Pedlar, A. 2006a, *AJ*, 132, 546
- Gallimore, J. F., Baum, S. A., & O’Dea, C. P. 2004, *ApJ*, 613, 794
- Gallimore, J. F., Elitzur, M., & Baum, S. A. 2006b, in *Physics of Active Galactic Nuclei at all Scales*, ed. D. Alloin, Vol. 693, 101
- Gallimore, J. F., Elitzur, M., Maiolino, R., et al. 2016, *ApJL*, 829, L7
- García-Burillo, S., Hicks, E. K. S., Alonso-Herrero, A., et al. 2024, *arXiv e-prints*, arXiv:2406.11398
- Garofalo, D., Evans, D. A., & Sambruna, R. M. 2010, *MNRAS*, 406, 975
- Ghisellini, G., & Tavecchio, F. 2009, *MNRAS*, 397, 985
- Ghosh, S., Kharb, P., Baghel, J., & Silpa, S. 2023, *ApJ*, 958, 71

- Gilli, R., Maiolino, R., Marconi, A., et al. 2000, *A&A*, 355, 485
- Giovanelli, R., Haynes, M. P., Rubin, V. C., & Ford, W. K., J. 1986, *ApJL*, 301, L7
- Giroletti, M., & Panessa, F. 2009, *ApJL*, 706, L260
- Hada, K., Doi, A., Nagai, H., et al. 2013, *ApJ*, 779, 6
- Harrison, C. M., & Ramos Almeida, C. 2024, *Galaxies*, 12, 17
- Heckman, T. M. 1980, *A&A*, 87, 152
- Heckman, T. M. 1987, in *Observational Evidence of Activity in Galaxies*, ed. E. E. Khachikian, K. J. Fricke, & J. Melnick, Vol. 121, 421
- Heckman, T. M., & Best, P. N. 2014, *ARA&A*, 52, 589
- Heckman, T. M., Kauffmann, G., Brinchmann, J., et al. 2004, *ApJ*, 613, 109
- Heinz, S., & Sunyaev, R. A. 2003, *MNRAS*, 343, L59
- Helou, G., Khan, I. R., Malek, L., & Boehmer, L. 1988, *ApJS*, 68, 151
- Ho, L. C. 1996, in *Astronomical Society of the Pacific Conference Series*, Vol. 103, *The Physics of Liners in View of Recent Observations*, ed. M. Eracleous, A. Koratkar, C. Leitherer, & L. Ho, 103
- Ho, L. C. 1999, *Advances in Space Research*, 23, 813
- 2008, *ARA&A*, 46, 475
- 2009, *ApJ*, 699, 626
- Ho, L. C., Rudnick, G., Rix, H.-W., et al. 2000, *ApJ*, 541, 120
- Homan, D. C., & Lister, M. L. 2006, *AJ*, 131, 1262
- Huchra, J., & Burg, R. 1992, *ApJ*, 393, 90
- Hummel, E., van der Hulst, J. M., & Dickey, J. M. 1984, *A&A*, 134, 207
- Irwin, J., Beck, R., Benjamin, R. A., et al. 2012, *AJ*, 144, 43
- Irwin, J. A., & Saikia, D. J. 2003, *MNRAS*, 346, 977
- Irwin, J. A., & Seaquist, E. R. 1988, *ApJ*, 335, 658
- Irwin, J. A., Schmidt, P., Damas-Segovia, A., et al. 2017, *MNRAS*, 464, 1333
- Irwin, J. A., Henriksen, R. N., Weźgowiec, M., et al. 2018, *MNRAS*, 476, 5057
- Ishibashi, W., & Courvoisier, T. J. L. 2011, *A&A*, 525, A118
- Jiang, Y., Li, J.-T., Gao, Y., et al. 2024, *MNRAS*, 528, 4160
- Jiménez-Benito, L., Díaz, A. I., Terlevich, R., & Terlevich, E. 2000, *MNRAS*, 317, 907
- Jones, S., McHardy, I., Moss, D., et al. 2011, *MNRAS*, 412, 2641
- Kale, R., Shende, K. M., & Parekh, V. 2019, *MNRAS*, 486, L80
- Kang, H., & Ryu, D. 2011, *ApJ*, 734, 18
- Kapferer, W., Sluka, C., Schindler, S., Ferrari, C., & Ziegler, B. 2009, *A&A*, 499, 87
- Kellermann, K. I., Sramek, R., Schmidt, M., Shaffer, D. B., & Green, R. 1989, *AJ*, 98, 1195
- Kennicutt, Robert C., J. 1998, *ARA&A*, 36, 189
- Khachikian, E. Y., & Weedman, D. W. 1974, *ApJ*, 192, 581
- Kharb, P., Blackman, E. G., Clausen-Brown, E., et al. 2024, *ApJ*, 962, 180
- Kharb, P., Hota, A., Croston, J. H., et al. 2010, *ApJ*, 723, 580
- Kharb, P., O’Dea, C. P., Baum, S. A., Colbert, E. J. M., & Xu, C. 2006, *ApJ*, 652, 177
- Kharb, P., O’Dea, C. P., Baum, S. A., et al. 2008, *ApJS*, 174, 74
- 2014, *MNRAS*, 440, 2976
- Kharb, P., Srivastava, S., Singh, V., et al. 2016, *MNRAS*, 459, 1310
- Kharb, P., Subramanian, S., Das, M., Vaddi, S., & Paragi, Z. 2021, *ApJ*, 919, 108
- King, A., & Pounds, K. 2015, *ARA&A*, 53, 115
- Kollatschny, W., & Fricke, K. J. 1985, *A&A*, 143, 393
- Krause, M., Irwin, J., Schmidt, P., et al. 2020, *A&A*, 639, A112
- Kukula, M. J., Pedlar, A., Baum, S. A., & O’Dea, C. P. 1995, *MNRAS*, 276, 1262
- Lähteenmäki, A., Järvelä, E., Ramakrishnan, V., et al. 2018, *A&A*, 614, L1
- Laing, R. A. 1980a, in *Bulletin of the American Astronomical Society*, Vol. 12, 823
- Laing, R. A. 1980b, *MNRAS*, 193, 439
- 1981, *ApJ*, 248, 87
- Laor, A. 2000, *ApJL*, 543, L111
- Laor, A., Baldi, R. D., & Behar, E. 2019, *MNRAS*, 482, 5513
- Laor, A., & Behar, E. 2008, *MNRAS*, 390, 847
- Lasota, J. P., Abramowicz, M. A., Chen, X., et al. 1996, *ApJ*, 462, 142
- Lavalley, M., Isobe, T., & Feigelson, E. 1992, in *Astronomical Society of the Pacific Conference Series*, Vol. 25, *Astronomical Data Analysis Software and Systems I*, ed. D. M. Worrall, C. Biemesderfer, & J. Barnes, 245
- Lebedev, S. V., Suttle, L., Swadling, G. F., et al. 2014, *Physics of Plasmas*, 21, 056305
- Li, J.-T., Sun, W., Ji, L., & Yang, Y. 2024, *ApJ*, 966, 239
- Li, J.-T., Wang, Q. D., Li, Z., & Chen, Y. 2011, *ApJ*, 737, 41
- Li, J.-T., Beck, R., Dettmar, R.-J., et al. 2016, *MNRAS*, 456, 1723
- Li, Y., Wang, D. X., & Gan, Z. M. 2008, *A&A*, 482, 1
- Liu, Y., Jiang, D. R., & Gu, M. F. 2006, *ApJ*, 637, 669

- Luminari, A., Marinucci, A., Bianchi, S., et al. 2023, *ApJ*, 950, 160
- Malkan, M. A., Gorjian, V., & Tam, R. 1998, *ApJS*, 117, 25
- Maoz, D. 2007, *MNRAS*, 377, 1696
- Marinucci, A., Bianchi, S., Braitto, V., et al. 2018, *MNRAS*, 478, 5638
- Matt, G., Baloković, M., Marinucci, A., et al. 2015, *MNRAS*, 447, 3029
- McLure, R. J., & Dunlop, J. S. 2001, *MNRAS*, 327, 199
- McLure, R. J., Willott, C. J., Jarvis, M. J., et al. 2004, *MNRAS*, 351, 347
- Meenakshi, M., Mukherjee, D., Bodo, G., & Rossi, P. 2023, *MNRAS*, 526, 5418
- Mehdipour, M., & Costantini, E. 2019, *A&A*, 625, A25
- Mehdipour, M., Kriss, G. A., Brenneman, L. W., et al. 2022, *ApJ*, 925, 84
- Meléndez, M., Kraemer, S. B., & Schmitt, H. R. 2010, *MNRAS*, 406, 493
- Merloni, A., & Fabian, A. C. 2002, *MNRAS*, 332, 165
- Merloni, A., & Heinz, S. 2007, *MNRAS*, 381, 589
- Mezcua, M., & Prieto, M. A. 2014, *ApJ*, 787, 62
- Middelberg, E., Agudo, I., Roy, A. L., & Krichbaum, T. P. 2007, *MNRAS*, 377, 731
- Miyaji, T., Wilson, A. S., & Perez-Fournon, I. 1992, *ApJ*, 385, 137
- Mizumoto, M., Done, C., Tomaru, R., & Edwards, I. 2019, *MNRAS*, 489, 1152
- Moran, E. C. 2000, *NewAR*, 44, 527
- Moshir, M., & et al. 1990, *IRAS Faint Source Catalogue*, 0
- Moshir, M., Copan, G., Conrow, T., et al. 1993, *VizieR Online Data Catalog: IRAS Faint Source Catalog, |b| > 10, Version 2.0 (Moshir+ 1989)*, *VizieR On-line Data Catalog: II/156A*. Originally published in: 1990IRASF.C.....0M, ,
- Mueller Sanchez, F., Malkan, M., Hicks, E., Shaver, S., & Ruby, M. 2022, in *American Astronomical Society Meeting Abstracts*, Vol. 240, American Astronomical Society Meeting #240, 112.03
- Mukherjee, D., Bicknell, G. V., Wagner, A. Y., Sutherland, R. S., & Silk, J. 2018, *MNRAS*, 479, 5544
- Mundell, C. G., Ferruit, P., Nagar, N., & Wilson, A. S. 2009, *ApJ*, 703, 802
- Nagao, T., Kawabata, K. S., Murayama, T., et al. 2004, *AJ*, 128, 109
- Nagar, N. M., Falcke, H., Wilson, A. S., & Ulvestad, J. S. 2002a, *A&A*, 392, 53
- Nagar, N. M., Oliva, E., Marconi, A., & Maiolino, R. 2002b, *A&A*, 391, L21
- Narayan, R., Mahadevan, R., Grindlay, J. E., Popham, R. G., & Gammie, C. 1998, *ApJ*, 492, 554
- Nikołajuk, M., Czerny, B., & Gurynowicz, P. 2009, *MNRAS*, 394, 2141
- Nolting, C., Jones, T. W., O’Neill, B. J., & Mendygral, P. J. 2019, *ApJ*, 876, 154
- O’Brien, P. C. 1978, *Biometrics*, 34, 243.  
<http://www.jstor.org/stable/2530014>
- O’Dea, C. P. 1998, *PASP*, 110, 493
- O’Dea, C. P., & Owen, F. N. 1987, *ApJ*, 316, 95
- O’Dea, C. P., & Saikia, D. J. 2021, *A&A Rv*, 29, 3
- Oosterloo, T., & van Gorkom, J. 2005, *A&A*, 437, L19
- Orienti, M., & Prieto, M. A. 2010, *MNRAS*, 401, 2599
- Pacholczyk, A. G. 1970, *Radio astrophysics* (
- Padovani, P. 2017, *Nature Astronomy*, 1, 0194
- Panessa, F., Baldi, R. D., Laor, A., et al. 2019, *Nature Astronomy*, 3, 387
- Peterson, B. M. 1997, *An Introduction to Active Galactic Nuclei*
- Phillips, M. M., & Malin, D. F. 1982, *MNRAS*, 199, 905
- Pogge, R. W. 1989, *ApJ*, 345, 730
- Pounds, K. A., & King, A. R. 2013, *MNRAS*, 433, 1369
- Proga, D., & Kallman, T. R. 2004, *ApJ*, 616, 688
- Punsly, B. 2005, *ApJL*, 623, L9
- Qian, Q., Fendt, C., & Vourellis, C. 2018, *ApJ*, 859, 28
- Radcliffe, J. F., Barthel, P. D., Garrett, M. A., et al. 2021, *A&A*, 649, L9
- Rafferty, D. A., McNamara, B. R., Nulsen, P. E. J., & Wise, M. W. 2006, *ApJ*, 652, 216
- Ramos Almeida, C., Levenson, N. A., Rodríguez Espinosa, J. M., et al. 2009, *ApJ*, 702, 1127
- Rao, V. V., Kharb, P., Rubinur, K., et al. 2023, *MNRAS*, 524, 1615
- Rau, U., & Cornwell, T. J. 2011, *A&A*, 532, A71
- Rawlings, S., & Saunders, R. 1991, *Nature*, 349, 138
- Readhead, A. C. S., Hough, D. H., Ewing, M. S., Walker, R. C., & Romney, J. D. 1983, *ApJ*, 265, 107
- Rees, M. J. 1984, *ARA&A*, 22, 471
- Robitaille, T. P., Rossa, J., Bomans, D. J., & van der Marel, R. P. 2007, *A&A*, 464, 541
- Rubin, V. C. 1978, *ApJL*, 224, L55
- Rush, B., Malkan, M. A., & Edelson, R. A. 1996, *ApJ*, 473, 130
- Rush, B., Malkan, M. A., & Spinoglio, L. 1993, *ApJS*, 89, 1
- Rybicki, G. B., & Lightman, A. P. 1979, *Radiative processes in astrophysics*
- Santoro, F., Tadhunter, C., Baron, D., Morganti, R., & Holt, J. 2020, *A&A*, 644, A54
- Santos-Lleo, M., Clavel, J., Barr, P., et al. 1995, *MNRAS*, 274, 1
- Sargent, A. J., Fischer, T. C., Johnson, M. C., et al. 2024, *ApJ*, 961, 230

- Saxton, C. J., Bicknell, G. V., Sutherland, R. S., & Midgley, S. 2005, *MNRAS*, 359, 781
- Schmitt, H. R., Donley, J. L., Antonucci, R. R. J., Hutchings, J. B., & Kinney, A. L. 2003, *ApJS*, 148, 327
- Schmitt, H. R., Ulvestad, J. S., Antonucci, R. R. J., & Kinney, A. L. 2001, *ApJS*, 132, 199
- Sebastian, B., Kharb, P., O’Dea, C. P., Colbert, E. J. M., & Baum, S. A. 2019a, *ApJ*, 883, 189
- Sebastian, B., Kharb, P., O’Dea, C. P., Gallimore, J. F., & Baum, S. A. 2019b, *MNRAS*, 490, L26
- . 2020, *MNRAS*, 499, 334
- Seyfert, C. K. 1943, *ApJ*, 97, 28
- Shapovalova, A. I., Popović, L. Č., et al. 2019, *MNRAS*, 485, 4790
- Sikora, M., Stawarz, L., & Lasota, J.-P. 2007, *ApJ*, 658, 815
- Silpa, S., Kharb, P., Harrison, C. M., et al. 2022, *MNRAS*, 513, 4208
- . 2021a, *MNRAS*, 507, 991
- Silpa, S., Kharb, P., Ho, L. C., & Harrison, C. M. 2023, *ApJ*, 958, 47
- Silpa, S., Kharb, P., O’Dea, C. P., et al. 2021b, *MNRAS*, 507, 2550
- Singh, V., Ishwara-Chandra, C. H., Wadadekar, Y., Beelen, A., & Kharb, P. 2015, *MNRAS*, 446, 599
- Stone, John L., J., Wilson, A. S., & Ward, M. J. 1988, *ApJ*, 330, 105
- Strickland, D. K., Heckman, T. M., Colbert, E. J. M., Hoopes, C. G., & Weaver, K. A. 2004, *ApJS*, 151, 193
- Talbot, R. Y., Bourne, M. A., & Sijacki, D. 2021, *MNRAS*, 504, 3619
- Taylor, R. D., Uttley, P., & McHardy, I. M. 2003, *MNRAS*, 342, L31
- Tchekhovskoy, A., & Bromberg, O. 2016, *MNRAS*, 461, L46
- THE CASA TEAM, Bean, B., Bhatnagar, S., et al. 2022, arXiv e-prints, arXiv:2210.02276
- Thompson, A. R., Clark, B. G., Wade, C. M., & Napier, P. J. 1980, *ApJS*, 44, 151
- Tran, H. D., Miller, J. S., & Kay, L. E. 1992, *ApJ*, 397, 452
- Ulvestad, J. S., Neff, S. G., & Wilson, A. S. 1987, *AJ*, 93, 22
- Ulvestad, J. S., & Wilson, A. S. 1984, *ApJ*, 285, 439
- Urry, C. M., & Padovani, P. 1995a, *PASP*, 107, 803
- . 1995b, *PASP*, 107, 803
- Ursini, F., Bassani, L., Malizia, A., et al. 2019, *A&A*, 629, A54
- van der Laan, H., & Perola, G. C. 1969, *A&A*, 3, 468
- van Moorsel, G., Kembell, A., & Greisen, E. 1996, in *Astronomical Society of the Pacific Conference Series*, Vol. 101, *Astronomical Data Analysis Software and Systems V*, ed. G. H. Jacoby & J. Barnes, 37
- Vargas, C. J., Walterbos, R. A. M., Rand, R. J., et al. 2019, *ApJ*, 881, 26
- Veilleux, S., Cecil, G., & Bland-Hawthorn, J. 2005, *ARA&A*, 43, 769
- Veilleux, S., Cecil, G., Bland-Hawthorn, J., et al. 1994, *ApJ*, 433, 48
- Veilleux, S., Shopbell, P. L., Rupke, D. S., Bland-Hawthorn, J., & Cecil, G. 2003, *AJ*, 126, 2185
- Veilleux, S., Tully, R. B., & Bland-Hawthorn, J. 1993, *AJ*, 105, 1318
- Véron-Cetty, M. P., & Véron, P. 2006, *A&A*, 455, 773
- Vietri, A., Järvelä, E., Berton, M., et al. 2022, *A&A*, 662, A20
- Vollmer, B., & Huchtmeier, W. 2003, *A&A*, 406, 427
- Wang, D.-X., Ye, Y.-C., Li, Y., & Ge, Z.-J. 2008, *MNRAS*, 385, 841
- Wardle, J. 2018, *Galaxies*, 6, 5
- Weaver, K. A., Meléndez, M., Mushotzky, R. F., et al. 2010, *ApJ*, 716, 1151
- Wehrle, A. E., & Morris, M. 1988, *AJ*, 95, 1689
- Willott, C. J., Rawlings, S., Blundell, K. M., & Lacy, M. 1999, *MNRAS*, 309, 1017
- Wilson, A. S., & Ulvestad, J. S. 1982, *ApJ*, 263, 576
- Wilson, A. S., & Willis, A. G. 1980, *ApJ*, 240, 429
- Woo, J.-H., & Urry, C. M. 2002, *ApJ*, 579, 530
- Xanthopoulos, E., Thean, A. H. C., Pedlar, A., & Richards, A. M. S. 2010, *MNRAS*, 404, 1966
- Xu, X., Wang, J., Li, Z., & Chen, Y. 2024, arXiv e-prints, arXiv:2406.08861
- Yang, Y., Li, J.-T., Wiegert, T., et al. 2024, *ApJ*, 966, 213
- Yun, M. S., Reddy, N. A., & Condon, J. J. 2001, *ApJ*, 554, 803
- Zakamska, N. L., & Greene, J. E. 2014, *MNRAS*, 442, 784
- Zanchettin, M. V., Feruglio, C., Massardi, M., et al. 2023, *A&A*, 679, A88
- Zheng, Y., Wang, J., Irwin, J., et al. 2022, *MNRAS*, 513, 1329

## 8. APPENDIX

We present here the radio-optical overlays for the four galaxies showing galactic emission along with AGN outflows.

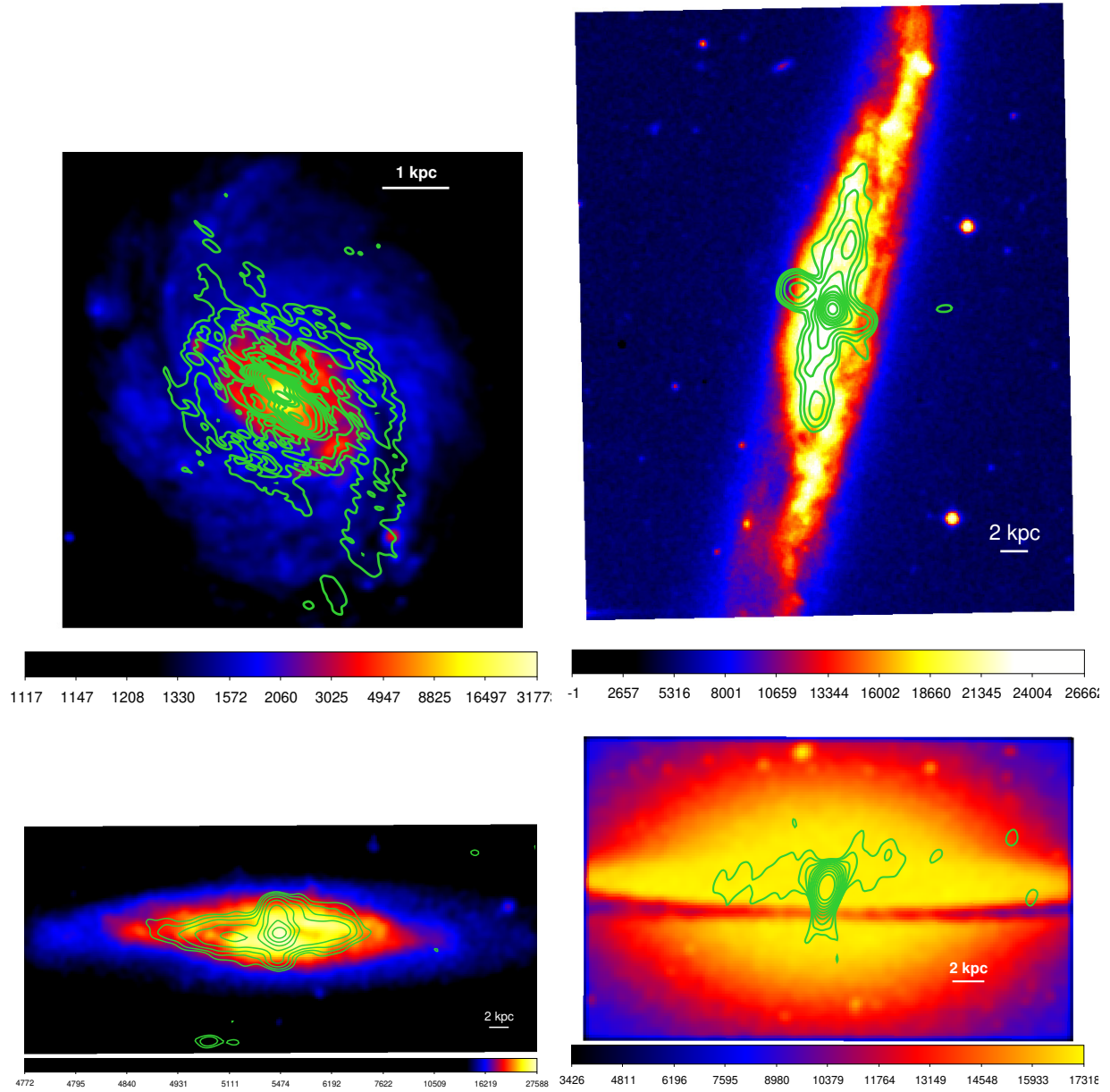


**Figure 21.** Radio-optical overlays for galaxies with observed galactic radio emission along with the Seyfert outflows. Galaxies shown clockwise from the left top are NGC 1068, NGC 3079, NGC 4594, and NGC 4388. 1.4 GHz (NGC 1068) or 10 GHz (NGC 3079, NGC 4388, NGC4594) radio contours in green superimposed on SDSS g-filter images of the host galaxies. The radio contour levels are  $3\sigma \times (-1, 1, 2, 4, 8, 16, 32, 64, 128, 256, 512)$  with  $\sigma = 250, 50, 20, 22 \mu\text{Jy beam}^{-1}$  for NGC 1068, NGC 3079, NGC 4594, and NGC 4388, respectively.